bioRxiv preprint doi: https://doi.org/10.1101/2020.10.08.331660; this version posted October 8, 2020. The copyright holder for this preprint (which was not certified by peer review) is the author/funder, who has granted bioRxiv a license to display the preprint in perpetuity. It is made available under aCC-BY-ND 4.0 International license.

Rapid Cortical Adaptation and the Role of Thalamic Synchrony During Wakefulness

Nathaniel C. Wright[1], Peter Y. Borden[1], Yi Juin Liew[2], Michael F. Bolus[1], William M. Stoy[3], Craig R. Forest[3], Garrett B. Stanley[1]

[1]Wallace H Coulter Department of Biomedical Engineering, Georgia Institute of Technology and Emory University, Atlanta, GA, USA

[2]Department of Biomedical Engineering, Georgia Institute of Technology, Emory University, Atlanta, GA, USA and Beijing University, Beijing China

[3] Department of Mechanical Engineering, Georgia Institute of Technology, Atlanta, Georgia, USA

Abbreviated Title: Cortical adaptation during wakefulness

With 44 text pages, 8 Figures

Correspondence: Garrett B Stanley

Coulter Department of Biomedical Engineering
Georgia Institute of Technology & Emory University
313 Ferst Drive
Atlanta GA 30332-0535
USA

Phone: 404-385-5037
Fax: 404-385-5044
Email: garrett.stanley@bme.gatech.edu

Conflict of Interest: The authors declare no competing financial interests.

Acknowledgements: We thank Aurelie Pala, Audrey Sederberg, Adam Willats, Christian Waiblinger, and Elaida Dimwamwa for helpful comments on the data analysis and manuscript. We thank Aurelie Pala for assistance with spike-sorting. **Funding**. This work was supported by NIH National Institute of Neurological Disorders and Stroke Grant R01 NS104928 (GBS), NIH National Institute of Mental Health U01MH106027 (GBS and CRF), NIH National Institute of Neurological Disorders and Stroke Pre-doctoral NRSA NS098691 (PYB), NIH National Eye Institute R01 EY023173 (CRF), and National Science Foundation Graduate Research Fellowships (WMS, MFB).

bioRxiv preprint doi: https://doi.org/10.1101/2020.10.08.331660; this version posted October 8, 2020. The copyright holder for this preprint (which was not certified by peer review) is the author/funder, who has granted bioRxiv a license to display the preprint in perpetuity. It is made available under aCC-BY-ND 4.0 International license.

Abstract

Rapid sensory adaptation is observed across all sensory systems, and strongly shapes sensory percepts in complex sensory environments. Yet despite its ubiquity and likely necessity for survival, the mechanistic basis is poorly understood. A wide range of studies primarily in in-vitro and anesthetized preparations have pointed to the emergence of adaptation effects at the level of primary sensory cortex, with only modest signatures in earlier stages of processing. The nature of rapid adaptation and how it shapes sensory representations during wakefulness, and thus the potential role in adaptive changes in perception, is unknown, as are the mechanisms that underlie this phenomenon. To address these unknowns, we recorded spiking activity in primary somatosensory cortex (S1) and the upstream ventral posteromedial (VPm) thalamic nucleus in the vibrissa pathway of the awake mouse, and quantified responses to whisker stimuli delivered in isolation and embedded in an adapting sensory background. We found that during wakefulness, cortical sensory responses were indeed adapted by persistent sensory stimulation; putative excitatory neurons were profoundly adapted, and inhibitory neurons only modestly so. Further optogenetic manipulation experiments and network modeling suggest this largely reflects adaptive changes in synchronous thalamic firing combined with robust engagement of feedforward inhibition, with little contribution from synaptic depression. Taken together, these results suggest that cortical adaptation largely reflects changes in timing of thalamic input, and the way in which this differentially impacts cortical excitation and feedforward inhibition, pointing to a prominent role of thalamic gating in rapid adaptation of primary sensory cortex.

Significance Statement

Rapid adaptation of sensory activity strongly shapes representations of sensory inputs across all sensory pathways over the timescale of seconds, and has profound effects on sensory perception. Despite its ubiquity and theoretical role in the efficient encoding of complex sensory environments, the mechanistic basis is poorly understood, particularly during wakefulness. In this study in the vibrissa pathway of awake mice, we show that cortical representations of sensory inputs are strongly shaped by rapid adaptation, and that this is mediated primarily by adaptive gating of the thalamic inputs to primary sensory cortex and the differential way in which these inputs engage cortical sub-populations of neurons.

bioRxiv preprint doi: https://doi.org/10.1101/2020.10.08.331660; this version posted October 8, 2020. The copyright holder for this preprint (which was not certified by peer review) is the author/funder, who has granted bioRxiv a license to display the preprint in perpetuity. It is made available under aCC-BY-ND 4.0 International license.

Introduction

Our experience of the world around us depends upon context. For instance, a noisy sensory environment provides persistent sensory stimulation, which can adaptively shape the representations of salient sensory features embedded within the environment. Rapid sensory adaptation describes such interactions between stimulus history and perception, spanning milliseconds to seconds. A wealth of human psychophysical studies have documented perceptual adaptation in audition (Bestelmeyer et al., 2010; Erb et al., 2013; Smith & Faulkner, 2006), vision (Anstis et al., 1998; C. Blakemore & Campbell, 1969; Colin Blakemore & Nachmias, 1971; Ghodrati et al., 2019), and somatosensation (Tannan et al., 2007), suggesting rapid sensory adaptation lends a vital flexibility to organisms tasked with surviving and thriving in the face of rapid environmental changes.

Despite its ubiquity across sensory systems and likely relevance to function and survival (Barlow, 1961), the neural basis for rapid sensory adaptation is unknown. A large body of (mostly in vitro and anesthetized) work has implicated primary sensory cortex in perceptual adaptation, by showing that persistent stimulation through sensory input or peripheral electrical stimulation adapts cortical responses in a manner suggestive of well documented perceptual effects. In the vibrissa pathway of the anesthetized rodent for example, adaptation induced through persistent whisker stimulation strongly shapes the amplitude (Cohen-Kashi Malina et al., 2013; Ganmor et al., 2010; Heiss et al., 2008; Kheradpezhouh et al., 2017; Ollerenshaw et al., 2014; Wang et al., 2010; Zheng et al., 2015) and spatial extent (Ollerenshaw et al., 2014; Zheng et al., 2015) of cortical responses to subsequent stimuli, with thalamic activity that serves as the input to S1 exhibiting significantly less adaptation by comparison (Chung et al., 2002; Khatri et al., 2004). Yet two important questions remain unanswered. First, how does rapid adaptation shape sensory representations during wakefulness, where baseline levels of activity are high relative to the anesthetized state (Aasebø et al., 2017; Greenberg et al., 2008; Vizuete et al., 2012)? It has been suggested that the thalamocortical pathway during wakefulness is in a baseline “adapted” state that is relatively impervious to additional adaptation (Castro-Alamancos, 2004), and the neural basis for perceptual adaptation lies elsewhere, but this has not been rigorously tested. Second, if indeed the circuit is subject to sensory adaptation during wakefulness, what are the underlying mechanisms? Although previous anesthetized and in-vitro work implicates thalamocortical and/or intracortical synaptic depression (Castro-Alamancos & Oldford, 2002; Chung et al., 2002; Cohen-Kashi Malina et al., 2013; Cruikshank et al., 2007, 2010; Gabernet et al., 2005), adaptation effects on thalamic properties such as population synchrony (Ollerenshaw et al., 2014; Wang et al., 2010) and single-unit bursting (Whitmire et al., 2016b) observed under anesthesia suggest a potential role for thalamus in shaping the adapted cortical response, given the high sensitivity of cortex to the timing

bioRxiv preprint doi: https://doi.org/10.1101/2020.10.08.331660; this version posted October 8, 2020. The copyright holder for this preprint (which was not certified by peer review) is the author/funder, who has granted bioRxiv a license to display the preprint in perpetuity. It is made available under aCC-BY-ND 4.0 International license.

of thalamic inputs (Bruno & Sakmann, 2006; Ollerenshaw et al., 2014; Swadlow & Gusev, 2001; Wang et al., 2010).

Here, we address these unknowns by recording from and modeling the primary somatosensory (S1) cortex of the awake, head-fixed mouse during rapid sensory adaptation. We found that despite the relatively high level of baseline activity typical of the awake state, putative excitatory neurons in S1 were profoundly adapted by a background sensory adapting stimulus. In particular, mean evoked firing rates, theoretical stimulus detectability, and synchronous cortical spiking were all significantly reduced in the adapted state, consistent with previously-reported decreases in detection performance. Several lines of evidence – including the recording of the thalamic inputs under a range of optogenetic controls and computational modeling – suggest this primarily reflected reduced synchronous thalamic firing and robust thalamically-driven feedforward inhibition in the adapted condition, with little contribution from thalamocortical and intracortical synaptic depression. Taken together, the results here establish the role of the thalamocortical circuit in rapid adaptation during wakefulness, and implicate a more critical role of thalamic input than previously thought.

bioRxiv preprint doi: https://doi.org/10.1101/2020.10.08.331660; this version posted October 8, 2020. The copyright holder for this preprint (which was not certified by peer review) is the author/funder, who has granted bioRxiv a license to display the preprint in perpetuity. It is made available under aCC-BY-ND 4.0 International license.

Materials and Methods

All procedures were approved by the Institutional Animal Care and Use Committee at the Georgia Institute of Technology (Protocol Numbers A100223 and A100225), and were in agreement with guidelines established by the National Institutes of Health.

Surgery

Mice were induced with 5% isoflurane in an induction chamber, then transferred to a heating pad on a stereotaxic instrument, and maintained at 1 - 2% isoflurane for the remainder of the surgical procedure. A custom stainless steel headplate was fixed to the exposed skull with Metabond dental cement (Parkell, Inc.), exposed bone and tissue were then sealed with Metabond and super-glue (Loctite 404; Henkel). Metabond was used to fashion a well surrounding the left hemisphere. The well was filled with Kwik-Cast (World Precision Instruments, Inc.) and covered with a thin layer of Metabond, and the mouse was returned to its home cage. Mice were given pre- (buprenorphine) and post-operative (ketoprofen) analgesic, and were allowed to recover for three days before additional handling.

Habituation

Three days after headplate implantation, mice were handled for at least 15 minutes, and then returned to their home cage. On subsequent days, mice were gradually habituated to head-fixation on a custom platform consisting of a tunnel with headpost clamps at one end. The first three daily habituation sessions lasted 15, 30, and 45 minutes respectively, but mice were returned to their home cage if they displayed signs of distress. We then gradually extended session durations until mice would tolerate at least 1.5 hours of fixation and whisker stimulation without signs of distress. Mice that did not meet these criteria were removed from the study, or used for anesthetized recordings (see below).

Awake electrophysiological recordings

We recorded from five Ai32 x nsmf-cre, four C57BL/6J (wild-type) and one Ai32xPV-cre awake mice (up to three awake sessions per mouse). We used intrinsic optical signal imaging acquired under anesthesia to identify at least one putative principal column in S1. On the morning of the first recording session for each animal, we anesthetized the mouse as described above, and opened an approximately 500 micron x 500 micron craniotomy centered over a putative cortical column. When acquiring simultaneous VPm

bioRxiv preprint doi: https://doi.org/10.1101/2020.10.08.331660; this version posted October 8, 2020. The copyright holder for this preprint (which was not certified by peer review) is the author/funder, who has granted bioRxiv a license to display the preprint in perpetuity. It is made available under aCC-BY-ND 4.0 International license.

and S1 recordings, we opened a second craniotomy of similar size over the stereotactic coordinates for VPm (1.8mm lateral from midline by 1.8mm caudal from bregma) and slowly inserted either a single-channel tungsten electrode (2 MOhm, FHC) or 32-channel silicon probe (NeuroNexus A1x32-Poly3-5mm-25s-177) to a depth of approximately 3 mm. We adjusted the depth while presenting continuous 10 Hz "sawtooth" stimulus trains to individual whiskers until we could identify a putative principal barreloid (by observing broad-waveform units with robust, short-latency, minimally-adapting sensory responses to stimulation of a single whisker, and at most comparatively weak responses to stimulation of surrounding whiskers (Brecht & Sakmann, 2002)), before slowly retracting the electrode/probe. We then covered exposed brain tissue with agarose, filled the well with Kwik-Cast, and allowed the mouse to recover in its home cage for at least two hours. After recovery, we head-fixed the awake mouse, removed the Kwik-Cast, filled the well with either saline, mineral oil, or agarose, and inserted an electrode/probe into each open craniotomy using a Luigs and Neumann manipulator. For S1 recordings, we inserted a multi-channel silicon probe (NeuroNexus) oriented 35 degrees from vertical. We used either a 32-channel linear (A1x32-5mm-25-177-A32), 32-channel "Poly3" (A1x32-Poly3-5mm-25s-177), or 64-channel, four-shank "Poly2" (A4x16-Poly2-5mm-23s-200-177) configuration probe. For VPm recordings, we inserted either a tungsten optoelectrode (2 Megaohm, FHC, with attached 200 micron optic fiber, Thorlabs), 32-channel silicon probe (A1x32-Poly3-5mm-25s-177) or 32-channel silicon optoelectrode (A1x32-Poly3-5mm-25s-177-OA32LP, with attached 105 micron optic fiber coupled to a 200 micron optic fiber, Thorlabs). Optic fibers were coupled to a 470 nm LED (M470F3, Thorlabs). When the barreloid we functionally identified during the anesthetized VPm mapping session was not topographically-aligned with the targeted S1 column, we referenced the (Coronal) Allen Brain Atlas to adjust the positioning of the VPm probe before descending. We inserted the probe(s) slowly to avoid excessive tissue dimpling, and waited at least 30 minutes after probe insertion to begin recording, to allow the tissue to settle. Continuous signals were acquired using a either a Cerebus (Blackrock Microsystems) or Tucker Davis Technologies acquisition system. Signals were amplified, filtered between 0.3 Hz and 7.5 kHz and digitized at either 30 kHz or 24414.0625 Hz.

After the first recording session, we removed the probe(s), covered exposed tissue with agarose, and sealed the well with Kwik-Cast and a thin layer of Metabond. We obtained either two or three recording sessions (one per day) from each mouse using the original craniotomy, but each time targeting a different cortical column and barreloid.

Anesthetized extracellular recordings

We recorded from three C57BL/6J (wild-type), four Ai32xPV-Cre, and three Ai32xnsmf mice under isoflurane anesthesia. Mice were anesthetized and implanted with

bioRxiv preprint doi: https://doi.org/10.1101/2020.10.08.331660; this version posted October 8, 2020. The copyright holder for this preprint (which was not certified by peer review) is the author/funder, who has granted bioRxiv a license to display the preprint in perpetuity. It is made available under aCC-BY-ND 4.0 International license.

205 headplates, and we opened a single craniotomy (either approximately 500 microns x 500
206 microns, or 1 mm x 1 mm) over S1, as described above. In some cases, the principal
207 column was first identified using intrinsic optical signal imaging, as described above. In
208 other cases, we inserted a single tungsten electrode into the stereotactic coordinates for
209 the center of S1, and defined the putative principal whisker to be that which evoked the
210 largest LFP response. We then inserted a 4 x 16 silicon probe array (A4x16-Poly2-5mm-
211 23s-200-177) to a depth of 700 microns. We oriented the probe to avoid blood vessels
212 on the cortical surface. For a subset of these experiments, we obtained additional
213 sessions by repeating the stimulation protocol using the whisker that evoked the
214 maximum LFP response on a shank different from the first. For each such session, we
215 determined the putative principal column off-line using white-noise-evoked spiking. For
216 each shank, we summed single- and multi-unit (see below) spiking across all trials for the
217 1 s window preceding feature onset. We divided the across-trial mean white-noise-
218 evoked response by the across-trial standard deviation of spontaneous spiking, and the
219 shank with the largest resulting value was determined to correspond to the principal
220 column.

221

222 *Anesthetized intracellular recordings*

223 We recorded ongoing, sensory-evoked, and light-evoked subthreshold activity from four
224 sensory- and light-responsive neurons in two mice using an Autopatcher system
225 (Kodandaramaiah et al., 2016), as described in detail previously (Stoy et al.,
226 2020). Briefly, we head-plated and identified the putative C2 column using intrinsic optical
227 signal imaging in two isoflurane-anesthetized Ai32 x NR133 transgenic mice, and opened
228 a 1 mm x 1 mm craniotomy over the column, as described above. We then used an
229 Autopatcher 1500 (Neuromatic Devices) to provide pressure and measure pipette
230 resistance, and an algorithm based on these measurements to navigate around blood
231 vessels in an automated fashion while the pipette descended through cortical tissue.
232 Finally, we applied a recently-developed automated motion-compensation procedure
233 (Stoy et al., 2020) for synchronizing the motion of the pipette tip to that of the targeted
234 neuron prior to forming the seal. These experiments utilized Multiclamp 700B amplifiers
235 (Molecular Devices), and signals were digitized at 20 kHz (cDAQ-9174, National
236 Instruments), and recorded in PClamp 10 in current-clamp mode.

237

238 *Whisker stimulation*

239 We used a precise, computer-controlled galvanometer (Cambridge Technologies) with
240 attached tube to stimulate individual whiskers (Sederberg et al., 2018; Whitmire et al.,
241 2016b). The galvanometer was controlled using either a custom Matlab GUI and Simulink

bioRxiv preprint doi: https://doi.org/10.1101/2020.10.08.331660; this version posted October 8, 2020. The copyright holder for this preprint (which was not certified by peer review) is the author/funder, who has granted bioRxiv a license to display the preprint in perpetuity. It is made available under aCC-BY-ND 4.0 International license.

Real-Time (Mathworks), or the Real-time eXperiment Interface application (http://rtxi.org/, CITE), sampling at 1 kHz. We inserted the whisker into the tube, which was positioned approximately 10 mm from the whisker pad. We delivered "sawtooth" stimulus features (exponential rise and decay waveforms lasting approximately 17 ms, with reported velocity defined by the average over the 8.5 ms rising phase (Wang et al., 2010)) either in isolation, or embedded in frozen sensory white noise (i.e., white noise waveforms that were identical across trials). To generate the white noise waveforms, the value at each time-step was drawn from a Gaussian distribution, and the resulting signal was lowpass-filtered at 100 Hz (3rd-order Butterworth (Waiblinger et al., 2015)). The reported amplitude of the white noise stimulus is the standard deviation of the Gaussian distribution. The white noise waveform around the feature waveform was dampened with an inverted Gaussian, with standard deviation 25.5 ms, or twice the duration of the sawtooth waveform.

The stimulus conditions were randomized across trials. The stimulus consisted of 1.5 s of either white noise ("adapted" trials) or no white noise ("control" trials), with the onset of the embedded feature at 1 s. The inter-trial interval was a random value (drawn from a uniform distribution) between 2 and 3 s. We typically obtained at least 100 trials per stimulus condition.

Optogenetic stimulation

In a subset of acute anesthetized experiments in Ai32 x NR133 transgenic mice, we stimulated thalamocortical terminals in S1 using blue (470 nm) light from an LED (ThorLabs), and recorded either spiking or subthreshold S1 responses. We positioned either a 200 or 400 micron optic fiber (ThorLabs) just above the exposed cortical surface, adjacent to the probe or patch pipette. Light pulses were either 10 ms or 15 ms in duration, and were delivered either in isolation or embedded in sensory white noise delivered to the whisker by the galvanometer. We titrated the light level at the beginning of each recording session to evoke cortical responses that were comparable in amplitude to those evoked by punctate whisker stimulation.

In a subset of awake experiments in Ai32 x NR133 transgenic mice, we presented the above sensory stimulus protocol, in addition to a set of "LED" trials in which we delivered a step input of 470 nm light to VPm beginning 1 s before and ending 0.5 s after the delivery of an isolated sawtooth whisker stimulus. The light was delivered via LED-coupled fiber attached to the electrode/probe (described above). We titrated the light level at the beginning of each recording session such that steady-state light-evoked firing rates in VPm (based on threshold crossings of high-pass-filtered voltage recordings) approximately matched those evoked by the white noise whisker stimulus.

bioRxiv preprint doi: https://doi.org/10.1101/2020.10.08.331660; this version posted October 8, 2020. The copyright holder for this preprint (which was not certified by peer review) is the author/funder, who has granted bioRxiv a license to display the preprint in perpetuity. It is made available under aCC-BY-ND 4.0 International license.

Spike-sorting

We sorted spikes off-line using KiloSort2 (https://github.com/MouseLand/Kilosort2) for clustering, and phy (https://github.com/cortex-lab/phy) for manual curation of clusters. During manual curation, clusters were either merged or separated based primarily on waveform distributions across the probe and cross-correlogram structure. We discarded as "noise" those clusters whose across-instance mean waveform did not resemble a characteristic spike on any channel. All remaining clusters were labeled as either single- or multi-units by downstream analysis (see below).

Units retained for analysis

We labeled each curated cluster as either a single- or multi-unit based on the signal-to-noise ratio (SNR) and inter-spike interval (ISI) distribution. For each cluster and recorded spike, we calculated the absolute voltage difference between the trough and subsequent peak (VTP) on each channel. We defined the SNR to be the across-trial mean VTP divided by the across-trial standard deviation, for the channel on which the mean VTP was greatest. Additionally, we calculated "ISI violation percentage" for each cluster using the autocorrelogram (ACG). We defined the violation percentage to be the percentage of spikes in the 0 - 1 ms ACG bin. We then defined a well-isolated single-unit to be a cluster with SNR greater than 4.0, and ISI violation percentage below 1%. All other clusters were classified as multi-units. In our anesthetized recording sessions, we used an alternate probe configuration, which was somewhat less well-suited to obtaining well-isolated units. We therefore slightly relaxed our inter-spike interval violation constraints for defining "well-isolated" units, to yield more RS and FS cells from these datasets (see Methods). This did not qualitatively change our results. For S1, we further segregated single-units into regular- and fast-spiking units based on the mean waveform. Again using the channel on which the waveform was largest, we calculated the time from trough to subsequent peak (TTP). We classified S1 units with TTP < 0.4 ms to be fast-spiking units, and all others to be regular-spiking (CITE). Waveforms were in general narrower for VPm units, consistent with previous work (Barthó et al., 2014). We therefore classified VPm "RS" cells as those with TTP > 0.3 ms, and excluded units with narrower waveforms, which likely originated from either the cell bodies or axon terminals of neurons in reticular thalamus (Barthó et al., 2014). For putative VPm units, we further required that the absolute peak of the PSTH of responses to isolated punctate stimuli occur between 2 and 10 ms of stimulus onset. Finally, when analyzing activity of single- and/or multi-units, we only included those units with at least 0.25 mean post-stimulus spikes per trial, and a significant change ($p < 0.05$, Wilcoxon signed-rank test) in firing rate after stimulus onset

bioRxiv preprint doi: https://doi.org/10.1101/2020.10.08.331660; this version posted October 8, 2020. The copyright holder for this preprint (which was not certified by peer review) is the author/funder, who has granted bioRxiv a license to display the preprint in perpetuity. It is made available under aCC-BY-ND 4.0 International license.

316 on control (unadapted) trials, using the weakest sawtooth stimulus delivered during that
317 recording session and 50 ms (30 ms) pre- and post-stimulus windows for S1 (VPm).
318

319 *Experimental Design and Statistical Analyses*

320 When comparing two sets of values (that were matched samples) across stimulus
321 conditions, we used the Wilcoxon signed-rank test (implemented in Python using the
322 wilcoxon function in the Scipy library), and Bonferroni-corrected resulting p-values for
323 multiple comparisons where applicable. When comparing two independent samples
324 (e.g., normalized response rates for RS and FS cells), we used the Kruskal-Wallis test
325 (implemented in Python using the kruskal function in the Scipy library).

326 For any analysis resulting in a single value for a given recording session calculated using
327 all trials (e.g., AUROC, mean synchronous spike rates, etc.), we tested for significance of
328 change across conditions by re-sampling trials with replacement, re-calculating the final
329 value for the re-sampled pseudo-data, and calculating the 95% confidence intervals
330 (Bonferroni-corrected if necessary) of the resulting distribution of values.

331 The number of cells and animals used to calculate each reported result is included in the
332 text of the Results section and/or figure captions.

333

334 *Analyses*

335 All analyses were performed using custom scripts in Python 3.0. The details of each
336 analysis are presented below.

337

338 *ROC analysis*

339 We calculated the theoretical detectability of sawtooth sensory features for each
340 recording session by applying ideal observer analysis (Ollerenshaw et al., 2014; Wang et
341 al., 2010) to the “population response” distributions for ongoing and feature-evoked
342 activity. First, for each trial, we summed the ongoing and evoked spike counts across all
343 RS and multi-units. For visualization, we then “z-scored” these population results by
344 dividing the value for each trial by the across-trial standard deviation of ongoing activity
345 for the unadapted condition. This re-scaling gives an intuitive sense of a single-trial
346 response “amplitude” (as a multiple of baseline activity), but does not affect the
347 detectability calculation. Next, for each stimulus condition, we calculated the across-trial
348 mean and standard deviation of the z-scored spike counts, and generated a population
349 response distribution by drawing 1000 samples from a gamma distribution parameterized
350 by these values (Wang et al., 2010). For each punctate stimulus velocity, we calculated

bioRxiv preprint doi: https://doi.org/10.1101/2020.10.08.331660; this version posted October 8, 2020. The copyright holder for this preprint (which was not certified by peer review) is the author/funder, who has granted bioRxiv a license to display the preprint in perpetuity. It is made available under aCC-BY-ND 4.0 International license.

the true- and false-positive rates for each threshold value between 0 and the maximum response amplitude, using steps of two standard deviations. We then generated the receiver operator characteristic (ROC) curve by plotting the set of true-positive values vs. the false-positive values. Finally, we quantified the theoretical detectability as the area under the ROC curve (AUROC). The trend in across-population mean AUROC was qualitatively unchanged when we used recorded population responses rather than parametrized gamma distributions.

Synchrony analysis

We calculated the population synchrony of feature responses for each recording session using the population grand cross-correlogram (CCG) of single- and multi-unit spiking. First, for each trial, unit, and spike, we calculated the relative time of all spikes from other simultaneously-recorded units in a +/- 20 ms window. We repeated this for all spikes, units, and trials, populating the grand CCG. We defined the population synchrony to be the proportion of spikes in the CCG in the +/- 7.5 ms window (Wang et al., 2010).

Tonic and burst VPm spikes

We classified spikes from well-isolated units in putative VPm as either burst or tonic based on criteria described previously (Whitmire et al., 2016b). Bursts consisted of two or more sequential spikes from a single unit. We required at least 100 ms of quiescence before the first spike in the burst. Subsequent spikes were included in the burst if they occurred at most 4 ms after the previous spike. These criteria are consistent with the timing of burst spikes resulting from de-inactivation of T-type calcium channels after prolonged hyperpolarization.

S1 membrane potential analysis

We removed action potentials from intracellular voltage recordings by first identifying spike times and interpolating between the values 2.5 ms before and 2.5 ms after the peak of the action potential. To identify spike times in each recording, we first calculated the first time derivative time of the membrane potential at each time step. Spike onsets were defined to be positive crossings of five standard deviations of this time series. For each onset, the spike peak time corresponded to the next time at which the time derivative was less than or equal to zero. After interpolation, we low-pass-filtered the resulting time series (100 Hz, 3rd order Butterworth). For sawtooth sensory and optogenetic terminal stimulation responses, we calculated the across trial mean subthreshold response

bioRxiv preprint doi: https://doi.org/10.1101/2020.10.08.331660; this version posted October 8, 2020. The copyright holder for this preprint (which was not certified by peer review) is the author/funder, who has granted bioRxiv a license to display the preprint in perpetuity. It is made available under aCC-BY-ND 4.0 International license.

amplitude, time-to-peak, and width, using the same method as described above for the LFP.

Thalamocortical network model

We constructed a simple model of the thalamocortical network using custom scripts written in Python 3.6.10. All code is freely available upon request. We modeled a single cortical barrel as a clustered network of excitatory and inhibitory single-compartment leaky integrate-and-fire (LIF) neurons, subject to excitatory synaptic inputs from a "barreloid" of VPm neurons, and well as excitatory non-thalamic inputs that were independent across cortical neurons. For each of the "control" and "adapted" conditions, we simulated 50 trials, each lasting 150 ms, with a time-step of 0.05 ms.

We modeled a single VPm barreloid as forty independent trains of tonic and burst spikes, drawn from the empirical VPm PSTHs. The ongoing and evoked rates for each neuron were drawn from a skewed gamma distribution, to mimic the broad firing rate distributions of VPm neurons previously reported (Bruno & Simons, 2002; D. J. D. Pinto et al., 2000; Wang et al., 2010; Whitmire et al., 2016b). Bursts were modeled as pairs of spikes with 2.5 ms ISI.

Non-zero thalamocortical (TC) synaptic weights were drawn from a broad distribution, to mimic the reported variability in TC synaptic strengths and/or efficacies (Bruno & Sakmann, 2006; Bruno & Simons, 2002; Cruikshank et al., 2007, 2010; Gabernet et al., 2005; Sermet et al., 2019). Mean initial TC synaptic strengths were the same for excitatory and inhibitory neurons (Sermet et al., 2019), but TC convergence was higher for inhibitory neurons (75% for inhibitories, 50% for excitatories), and VPm neurons with the highest firing rates did not synapse onto excitatories (Bruno & Simons, 2002). In response to a spike in a given thalamic neuron, all TC synapses from that neuron instantly decayed (by a factor of 0.75), followed by exponential recovery (with time constant 25 ms).

We modeled a single cortical column as a network of 800 excitatory and 100 inhibitory LIF neurons, with relatively strong inhibitory-to-excitatory synapses (Gabernet et al., 2005). We imposed spatial clustering via "small-world" network connectivity (Bujan et al., 2015; Litwin-Kumar & Doiron, 2012; Wright, Hoseini, & Wessel, 2017; Wright, Hoseini, Yasar, et al., 2017), with 10% re-wiring probability. Inhibitory LIF neurons had shorter membrane time constants (Gentet et al., 2010) and refractory periods (1 ms for inhibitory, 2 ms for excitatory), which – together with the TC connection properties described above – supported higher firing rates in inhibitory neurons, as observed here during wakefulness (Fig. 1D – F) and in previous work (Bruno & Simons, 2002; Gentet et al., 2010; Khatri et al., 2004; Taub et al., 2013). Excitatory neurons were subject to an inhibitory spike-rate adaptation conductance, which helped to stabilize network activity.

bioRxiv preprint doi: https://doi.org/10.1101/2020.10.08.331660; this version posted October 8, 2020. The copyright holder for this preprint (which was not certified by peer review) is the author/funder, who has granted bioRxiv a license to display the preprint in perpetuity. It is made available under aCC-BY-ND 4.0 International license.

We quantified model responses by calculating the peaks of the grand PSTHs for excitatory and inhibitory LIF neurons and divided "adapted" values by "control" values, yielding the normalized adapted response. We generated grand cross-correlograms (as described above) for 200 randomly-selected excitatory-excitatory and inhibitory-inhibitory pairs, and for 100 VPm-VPm pairs.

We further employed two alternate models to parse the roles played by synchronous thalamic spikes and feedforward inhibition. For the "reduced synch" model, we maintained the mean spike rates of the original model, but manually adjusted drawn VPm spike times to reduce synchrony. Specifically, if a drawn VPm spike time was within +/- 5 ms of the empirical PSTH peak time, we shifted the spike to a random later time, within approximately 20 ms of the PSTH peak. For the "Identical TC Connectivity" model, excitatory and inhibitory neurons had the same TC convergence values (50%), and we did not require that VPm neurons with the highest rates synapse exclusively onto inhibitory neurons.

bioRxiv preprint doi: https://doi.org/10.1101/2020.10.08.331660; this version posted October 8, 2020. The copyright holder for this preprint (which was not certified by peer review) is the author/funder, who has granted bioRxiv a license to display the preprint in perpetuity. It is made available under aCC-BY-ND 4.0 International license.

Results

To investigate the adaptive effects of persistent sensory stimulation on S1 sensory responses during wakefulness, we presented precise deflections to a single whisker of the awake, head-fixed mouse using a computer controlled galvanometer, and recorded extracellular spiking activity in the corresponding principal column of S1, and/or principal barreloid of VPm. (Fig. 1A, see Methods). We presented punctate "sawtooth" whisker deflections either in isolation or embedded in an adapting background stimulus (frozen sensory white noise, Fig. 1A). The punctate stimuli capture the basic nature of the high velocity "stick-slip" whisker motion events that occur as a result of whisker contacts with larger surface irregularities during active sensation (Jadhav et al., 2009; Jadhav & Feldman, 2010; Ritt et al., 2008; Wolfe et al., 2008). During whisker contacts with surfaces, these stick-slip events are embedded in patterns of smaller-amplitude, irregular deflections (Jadhav & Feldman, 2010), simplistically captured here utilizing low-amplitude, repeatable white noise whisker stimulation (Waiblinger et al., 2015; Whitmire et al., 2016b). We first characterized the effects of the background stimulus on baseline and sawtooth-evoked cortical firing during wakefulness (Figs. 1 – 3), and then sought to identify the mechanisms underlying these effects through a battery of additional experiments (Figs. 4 – 7) and thalamocortical network modeling (Fig. 8).

S1 exhibits profound and differential sensory adaptation during wakefulness.

Before directly assessing the adaptive effects of the background stimulus, we characterized its effects on the rate and timing of baseline spiking activity in S1. We segregated well-isolated, sensory-responsive cortical units into regular-spiking (RS, putative excitatory) and fast-spiking (FS, putative inhibitory) neurons (Fig. 1B, see Methods). Sensory white noise noticeably elevated spiking activity in S1 in the form of stimulus-locked spiking, particularly among FS cells (Fig. 1C, D). We compared firing rates during presentation of the background stimulus to those during spontaneous activity (i.e., in the absence of stimulus delivery). We found that the stimulus significantly elevated the firing rates of both RS and FS units, with a more pronounced effect on FS rates (Fig. 1D). This differential effect is consistent with previous working demonstrating the higher sensitivity of S1 FS cells to relatively weak re-afferent excitatory drive during whisking (Gutnisky et al., 2017; Yu et al., 2016, 2019).

Next, we next investigated the adaptive effects of the background stimulus during wakefulness. To this end, we delivered 300 deg/s "sawtooth" punctate deflections to a single whisker, either in isolation (the "control" condition), or following 1 s of background stimulation (the "adapted" condition, Fig. 1A, see Methods). To investigate the relevance of adaptation across a range of punctate stimulus strengths, we delivered both moderate

bioRxiv preprint doi: https://doi.org/10.1101/2020.10.08.331660; this version posted October 8, 2020. The copyright holder for this preprint (which was not certified by peer review) is the author/funder, who has granted bioRxiv a license to display the preprint in perpetuity. It is made available under aCC-BY-ND 4.0 International license.

(300 deg/s) and relatively strong (900 deg/s) punctate stimuli in a subset of experiments. To avoid distortion of the punctate stimulus waveform, the background sensory white noise was dampened with an inverted Gaussian waveform in the neighborhood of the punctate stimulus (Waiblinger et al. 2015; Whitmire et al. 2016; see Methods). In the control condition, punctate deflections of both velocities evoked robust, short-latency spiking responses, (Fig. 1E), consistent with previous work in the anesthetized (Bruno & Simons, 2002; Khatri et al., 2004; D. J. Pinto et al., 2003; Wang et al., 2010) and awake (Musall et al., 2014) rodent. We next asked whether the background stimulus appreciably adapted punctate stimulus responses, or whether the relatively high baseline firing rates during wakefulness (Fig. 1D) resulted in a "pre-adapted" circuit (Castro-Alamancos, 2004). We found that S1 responses were in fact substantially muted when punctate stimuli were embedded in the background stimulus (Fig. 1E). To characterize RS and FS sensory responses and the effects of adaptation, we calculated across-trial mean evoked rates using a 50 ms window following punctate stimulus onset. For both cell types and punctate stimulus strengths, the peak (Fig. 1E) and mean (Fig. 1F) evoked rates were reduced in the adapted condition. Interestingly, adaptation appeared to be more profound for RS cells, in terms of proportional changes in sensory responses (Fig. 1E, F). To further quantify the effects of adaptation on a cell-by-cell basis, and to capture cell-type-specific adaptation, we calculated the normalized adapted response for each cell (i.e., the across-trial mean adapted response rate divided by the mean control rate, see Methods). For both punctate stimulus strengths and cell types, population median normalized adapted responses were less than one (capturing the general adaptive reduction in evoked rate), and RS cells were indeed significantly more adapted than FS cells (Fig. 1G). This differential effect was not specific to any cortical depth (Fig. 1H).

In summary, rapid sensory adaptation was observed in S1 of the awake mouse, and cortical putative excitatory neurons were more adapted than inhibitory neurons.

Adaptation reduces the theoretical detectability of punctate sensory stimuli.

We next addressed the potential implications of this response adaptation for the detectability of the punctate stimulus. To do so, we adopted a signal detection theory framework (Fig. 2A) to calculate the theoretical detectability of the stimulus in the control and adapted conditions. Qualitatively, the theoretical detectability of the stimulus is inversely related to the degree of overlap between the ongoing ("no-stim") and evoked ("stim") distributions (Fig. 2A, right). For each recording session, we generated ongoing and evoked population spiking distributions using the summed RS and multi-unit spike counts for each trial (Fig. 2B, see Methods). For this analysis, we excluded putative inhibitory neurons, as we were interested in interpreting the loss of excitatory drive from cortical neurons. We included multi-units to yield better-populated response distributions.

bioRxiv preprint doi: https://doi.org/10.1101/2020.10.08.331660; this version posted October 8, 2020. The copyright holder for this preprint (which was not certified by peer review) is the author/funder, who has granted bioRxiv a license to display the preprint in perpetuity. It is made available under aCC-BY-ND 4.0 International license.

While this likely introduced contributions from inhibitory neurons, this would tend to diminish the effects of adaptation on theoretical detectability, as FS units were less profoundly adapted (Fig. 1). Consistent with the overall adaptive decrease in single-neuron response rates (Fig. 1F), adaptation tended to move the evoked distribution toward the ongoing distribution, increasing the degree of overlap (Fig. 2B, right). We quantified the overlap by calculating the area under the receiver operator characteristic curve (Wang et al., 2010; Whitmire et al., 2016b) (AUROC, Fig. 2C), which has a value of 1.0 for non-overlapping distributions, and 0.5 for complete overlap. According to this measure, sensory white noise reduced the across-session mean detectability of the sawtooth stimulus by 16.3% (Fig. 2D, bottom). Thus, adaptation significantly reduced the theoretical detectability of punctate whisker stimuli, consistent with previous recordings in S1 of the anesthetized rat (Ollerenshaw et al., 2014; Wang et al., 2010; Zheng et al., 2015), and adaptive changes in behavior in awake rats (Ollerenshaw et al., 2014).

Adaptation increases the latency of and reduces synchronous spiking in S1 sensory responses

Besides the adaptation of mean evoked rates (Fig. 1F, G), visual inspection of the grand PSTHs (Fig. 1E) suggests an apparent increase in the latency of responses in the adapted condition, as well as a dramatic reduction in evoked rates in the early response (particularly among RS cells). These phenomena may be relevant for interpreting the mechanistic basis of S1 adaptation, and the likely perceptual implications; both are consistent with weaker feedforward excitatory drive to S1, and the latter could impair the ability of S1 RS cells to drive downstream targets. We therefore sought to quantify these adaptive effects and began by calculating response latency on a cell-by-cell basis. However, in contrast to the relatively well-populated grand PSTHs (Fig. 2C), the sparsely-populated PSTHs of individual neurons confound response onset calculations (Fig. 3A, left). As such, we convolved the spike trains of each neuron with a Gaussian kernel, yielding a convolved aggregate spike count time series ($\tilde{s}$, Fig. 3A, right, see Methods), or a smoothed PSTH. We defined the response onset (T_{onset}) for each stimulus condition to be the time at which $\tilde{s}$ exceeded four standard deviations of the pre-stimulus values (calculated from control trials). We found that for both RS and FS cells, and for both stimulus strengths, adaptation increased T_{onset} values (Fig. 3B). To further quantify and compare adaptive changes in T_{onset} across cell types, we calculated the T_{onset} adaptation index for each cell (see Methods) and compared population medians for RS and FS cells. For both stimulus strengths, the adaptive increase in response onset times was significantly greater for RS cells (300 deg/s RS median T_{onset} AI = 0.21, FS median T_{onset} AI = 0.02, $p = 1.21 \times 10^{-4}$, Kruskal-Wallis test; 900 deg/s RS median T_{onset} AI = 0.13, FS median T_{onset} AI = 0.00, $p = 4.93 \times 10^{-4}$).

bioRxiv preprint doi: https://doi.org/10.1101/2020.10.08.331660; this version posted October 8, 2020. The copyright holder for this preprint (which was not certified by peer review) is the author/funder, who has granted bioRxiv a license to display the preprint in perpetuity. It is made available under aCC-BY-ND 4.0 International license.

Next, we reasoned that the profound loss of evoked spikes in the early adapted S1 response (Fig. 1E) might reflect a decrease in synchronous spiking among cortical neurons. In general, the degree of synchronous firing among a population of neurons is likely related to the effect on synaptic targets; stronger inhibitory synchrony will tend to silence postsynaptic neurons, and stronger excitatory synchrony will be more efficacious for postsynaptic neurons – possibly downstream from S1. Indeed, it has been shown that coordinated population firing is a better predictor than mean rates of stimulus identity (Jadhav et al., 2009; Safaai et al., 2013; Zuo et al., 2015) and behavioral stimulus discrimination performance (Safaai et al., 2013; Zuo et al., 2015) when rodents whisk across textured surfaces.

To calculate the prevalence of synchronous spikes, we populated the grand cross-correlogram (CCG) for RS-RS and FS-FS pairs for each stimulus condition using spike trains from all pairs of simultaneously-recorded responsive cells, and defined synchronous spikes to be those within a +/- 7.5 ms window around zero lag (Fig. 3C, see Methods, Wang et al. 2010). We found that adaptation drastically reduced the amplitude and sharpness of the RS-RS CCGs (Fig. 3D), while more modestly reducing the grand CCG amplitude for FS-FS pairs (Fig. 3E). This represented a significant decrease in synchronous spike counts for both pair types and stimulus velocities (Fig. 3G, see Methods for definition of “valid pairs”). As reflected in the grand CCGs, the decrease in FS-FS synchrony was significant, but proportionally smaller than that of RS-RS synchrony (compare Figs. 3F and 3G).

Thus, rapid sensory adaptation in S1 during wakefulness not only altered mean evoked spike rates (Fig. 1), and theoretical stimulus detectability (Fig. 2), but also response latencies and the prevalence of synchronous cortical spiking. In both cases, as with mean evoked rates (Fig. 1G), the adaptive effect on RS cells was more dramatic. The loss of synchronous excitatory firing has implications for the driving of targets downstream of S1, and ultimately for perception and behavior. The more modest decrease in synchronous inhibitory firing implies that inhibitory neurons were still relatively strongly driven in the adapted condition. Further, the synchronous inhibitory spiking that survives adaptation should provide robust feedforward inhibition to S1 excitatory neurons, which may in part explain the more profound adaptation of RS cells.

S1 sensory responses are also adapted under anesthesia, but RS cells are not differentially adapted

Having established the existence and characteristics of rapid sensory adaptation in S1 of the awake mouse (Figs. 1 – 3), we next turned our attention to the underlying mechanisms. Our first step in doing so was to compare these results to those from the

bioRxiv preprint doi: https://doi.org/10.1101/2020.10.08.331660; this version posted October 8, 2020. The copyright holder for this preprint (which was not certified by peer review) is the author/funder, who has granted bioRxiv a license to display the preprint in perpetuity. It is made available under aCC-BY-ND 4.0 International license.

anesthetized mouse, for two reasons. First, while the background stimulus elevated S1 firing rates at least in part via feedforward sensory inputs (as evidenced by the degree of stimulus-locked firing, Fig. 1), it is still possible that this adapting stimulus also evoked top-down modulation, e.g., via systematic changes in ongoing S1 state via arousal-related, brainstem-mediated neuromodulation (Mcginley et al., 2015; McGinley et al., 2015; Reimer et al., 2014, 2016) and/or inputs from secondary motor area (Manita et al., 2015). In the anesthetized mouse, ongoing state changes caused by endogenous processes should be independent of the sensory white noise, and as such, white-noise-induced changes in mean punctate stimulus representations should not reflect top-down mechanisms. Second, isoflurane anesthesia tends to silence the secondary posteromedial nucleus of thalamus (Suzuki & Larkum, 2020), lowers baseline cortical firing rates (Aasebø et al., 2017; Greenberg et al., 2008; Vizuete et al., 2012), and generally weakens cortical inhibition (Haider et al., 2013) and other intracortical interactions (Suzuki & Larkum, 2020). We therefore repeated our experiments in a different set of mice lightly-anesthetized with isoflurane, using the anesthesia to unmask the feedforward inputs from VPm to S1.

As expected, baseline firing rates under anesthesia were quite low compared to those recorded during wakefulness (Fig. 4B, C). Despite these differences in baseline activity, the anesthetized experiments recapitulated several key aspects of the awake data. First, the background stimulus elevated baseline RS and FS firing rates (Fig. 4B, C), in the form of stimulus-locked spikes (Fig. 4B). Further, adaptation clearly decreased the peak (Fig. 4D) and mean evoked firing rates of responses to 300 deg/s punctate stimuli (Fig. 4E), and qualitatively shifted PSTHs to higher response latencies (Fig. 4D). One notable difference between the anesthetized and awake sessions was that excitatory neurons were not differentially adapted under anesthesia (Fig. 4F). In light of this, it is possible that the stronger cortical inhibition typical of wakefulness (Haider et al., 2013) contributed to adaptation of RS cells in our awake recordings via robust feedforward inhibition, such that RS adaptation was more profound during wakefulness than would be predicted from FS adaptation.

In summary, the elevation of (stimulus-locked) firing with presentation of background sensory stimulation, and net adaptation of S1 punctate stimulus responses was robust to anesthesia, suggesting that feedforward mechanisms explain these phenomena. In contrast, the differential adaptation of S1 excitatory neurons was abolished by anesthesia, suggesting the set of mechanisms underlying this phenomenon – possibly including strong feedforward inhibition – were not all active in the anesthetized state.

Adaptation reduces tonic and burst rates, and synchronous spiking, in VPm sensory responses

bioRxiv preprint doi: https://doi.org/10.1101/2020.10.08.331660; this version posted October 8, 2020. The copyright holder for this preprint (which was not certified by peer review) is the author/funder, who has granted bioRxiv a license to display the preprint in perpetuity. It is made available under aCC-BY-ND 4.0 International license.

Having established that several aspects of S1 sensory adaptation may be due to feedforward mechanisms, we next sought to identify those mechanisms. Based on previous work in slice and under anesthesia, we reasoned that our results largely represented some combination of adaptation of VPm sensory responses and activity-dependent depression of thalamocortical and intracortical synapses. Specifically, repetitive stimulation has been shown to reduce VPm sensory response spike rates (Ganmor et al., 2010; Hartings et al., 2003; Khatri et al., 2004; Liu et al., 2017; Ollerenshaw et al., 2014; Wang et al., 2010; Whitmire et al., 2016a), single-unit bursting (Whitmire et al., 2016b) and population synchrony (Ollerenshaw et al., 2014; Wang et al., 2010) in the anesthetized rodent, while also likely depressing the thalamocortical synapse (Castro-Alamancos & Oldford, 2002; Chung et al., 2002; Gabernet et al., 2005). Can these mechanisms explain S1 adaptation during wakefulness, and if so, what is the relative contribution of each?

As a first step toward addressing these questions, we repeated our experiments while recording extracellular spiking activity in VPm of the awake mouse (Fig. 5A, see Methods). As in S1, we found that the background stimulus significantly elevated firing rates in VPm (Fig. 5B, C) in the form of stimulus-locked spikes (Fig. 5B). We then characterized VPm responses to punctate stimuli, and the effects of the background stimulus on these responses. We first parsed VPm spikes into tonic and putative T-type calcium channel burst spikes ((Whitmire et al., 2016b), Fig. 5D). Bursts are groups of two or more spikes with very short inter-spike intervals, which have been shown to provide potent synaptic drive to S1 (Sherman, 2001; Swadlow, 2002; Swadlow & Gusev, 2001), and may therefore be critical for shaping cortical sensory responses. However, there is some disagreement as to whether VPm bursting occurs during wakefulness, when VPm is likely to be on average relatively depolarized. We did, in fact, observe sensory-evoked bursting, though burst spikes constituted a minority of total evoked spikes (Fig. 5E). Further, the punctate stimulus evoked both a short-latency primary peak, and a shorter, secondary peak in tonic firing rates (Fig. 5E). This secondary peak in the grand PSTH resulted from a subset of neurons with both early and late responses – often within individual trials – and was likely evoked by the return of the whisker to resting position in the second half of the sawtooth waveform. Next, we found that background stimulation reduced sawtooth-evoked rates for both tonic and burst spikes (Fig. 5E, F). While the reduction in overall evoked rate was qualitatively modest in comparison to that of downstream S1 RS cells (Fig. 1E, F), it has been shown that firing in S1 neurons depends not only on VPm rate, but on the relative timing of VPm spikes, as near-coincident spikes in pairs of VPm neurons may be required to effectively drive cortical targets (Bruno & Sakmann, 2006). We therefore next asked how the rate of synchronous VPm spikes changed with adaptation. To do this, we generated grand CCGs and calculated

bioRxiv preprint doi: https://doi.org/10.1101/2020.10.08.331660; this version posted October 8, 2020. The copyright holder for this preprint (which was not certified by peer review) is the author/funder, who has granted bioRxiv a license to display the preprint in perpetuity. It is made available under aCC-BY-ND 4.0 International license.

678 synchronous spike counts for each stimulus condition, as done previously for S1 RS cells
679 (Fig. 3). As in S1, we found that VPm synchronous spike counts were qualitatively a
680 better indicator than mean evoked rates of stimulus velocity (compare Figs. 5F and 5H),
681 consistent with previous work in anesthetized rat (Wang et al., 2010). Further, adaptation
682 significantly and substantially decreased synchronous VPm spike counts for both
683 deflection velocities (Fig. 5G, H)
684
685 In summary, adaptation in VPm (Fig. 5) was consistent with that observed in downstream
686 S1 (Figs. 1 – 3) during wakefulness. This suggests S1 response adaptation is inherited
687 to some degree directly from VPm, and in particular represents an adaptive decrease in
688 synchronous VPm spiking. Further, our recordings in S1 suggest that cortical RS cells
689 are particularly sensitive to changes in synchronous VPm spiking when baseline and
690 evoked inhibitory rates are elevated (as is the case during wakefulness).
691
692 **Optogenetic elevation of baseline VPm firing rate does not adapt S1 sensory**
693 **responses**
694
695 While VPm response adaptation predicted weaker excitatory drive to S1, it is also
696 possible that the background stimulus depressed thalamocortical and/or intracortical
697 synapses by elevating baseline firing rates, and therefore adapted S1 responses to a
698 greater degree than that predicted by evoked VPm rate alone. What were the relative
699 contributions of thalamic adaptation and synaptic depression? We sought to disentangle
700 these two candidate mechanisms by elevating baseline VPm rates without adapting VPm
701 sensory responses. To accomplish this, we utilized a transgenic mouse (Ai32 x Nsmf-
702 Cre) expressing Channelrhodopsin in VPm/VPl cell bodies, axons, and thalamocortical
703 axon terminals. We inserted either a tungsten or a 32-channel silicon optoelectrode into
704 VPm of the awake mouse for recording and optogenetic manipulation of thalamic spiking,
705 and a linear silicon probe into the topographically-aligned column of S1 (Fig. 6A, see
706 Methods).
707
708 As shown above separately for S1 (Fig. 1) and VPm (Fig. 5B, C), background sensory
709 stimulation evoked stimulus-locked firing in simultaneously-recorded VPm and S1 units
710 (Fig. 6B, left). On “LED” trials, we artificially elevated baseline VPm rates by substituting
711 the sensory white noise with step input of blue light to thalamus (Fig. 6B, right). We
712 titrated the light power such that mean baseline thalamic rates were comparable to “white
713 noise” trials (Fig. 6B, 6C, bottom). Interestingly, this did not significantly increase
714 downstream S1 firing rates above spontaneous levels, despite elevation of VPm rate (Fig.
715 6B, C, top), consistent with the notion that synchronous thalamic spikes (in this case,
716 evoked by sensory white noise) are required to effectively drive cortical targets (Bruno &
717 Sakmann, 2006).

bioRxiv preprint doi: https://doi.org/10.1101/2020.10.08.331660; this version posted October 8, 2020. The copyright holder for this preprint (which was not certified by peer review) is the author/funder, who has granted bioRxiv a license to display the preprint in perpetuity. It is made available under aCC-BY-ND 4.0 International license.

We next inspected the effects of our manipulations on VPm and S1 responses to 300 deg/s punctate whisker deflections. We were interested in the presence or absence of gross adaptive effects, and so we grouped together tonic and burst spikes in VPm, and RS and FS cells in S1 for this analysis. On LED trials, we maintained a constant light level during presentation of the sensory stimulus, to avoid transient VPm responses to reduction in light power. As shown above separately for S1 (Fig. 1) and VPm (Fig. 5), background sensory stimulation adapted simultaneously recorded responses in S1 (Fig. 6D, bottom). We next inspected the effects of optogenetically-elevated baseline VPm rates on sensory responses. If the "artificial" elevation of baseline VPm rate adapted TC synapses prior to delivery of the punctate sensory stimulus, we would anticipate adapted S1 sensory responses on LED trials, despite the non-adapted VPm sensory response (Fig. 6D, bottom). On the contrary, we observed no significant differences in S1 sensory response rates between the control and LED conditions (Fig. 6D, top), suggesting optogenetic elevation of baseline VPm rates did not appreciably adapt TC synapses. Importantly, LED presentation did not significantly enhance synchronous spike counts in the VPm sensory response relative to control trials (Fig. 6E), thus ruling out the possible confound of enhanced sensory-evoked thalamic synchrony masking the effects of synaptic depression.

To conclude, these manipulation experiments suggest that although background sensory stimulation elevates baseline VPm rates, this does not appreciably depress TC synapses, and other mechanisms underlie the adaptation of S1 responses to punctate whisker deflections.

S1 responses to direct terminal stimulation are only weakly adapted by sensory white noise

In the above experiments, baseline S1 rates were not significantly elevated on LED trials (Fig. 6C, top). In contrast, the background sensory stimulus significantly elevated baseline S1 firing (Fig. 6C, top), before presentation of the punctate stimulus. This leaves open the possibility that the adaptive effects of the background stimulus were largely due to intracortical synaptic depression, which was induced by the sensory white noise, but not the LED. Further, evoked VPm rates were slightly higher on LED trials than on control trials (Fig. 6D, bottom). It is possible then, that synapses were depressed on LED trials, but that the elevation in evoked VPm rate counteracted these adaptive effects. To address these potential confounds, we sought to more directly compare synaptic strengths in the absence and presence of background sensory stimulation. To do this, we took advantage of the expression of Channelrhodopsin in thalamocortical axon terminals of our transgenic mouse. We positioned an LED-coupled optic fiber above the

bioRxiv preprint doi: https://doi.org/10.1101/2020.10.08.331660; this version posted October 8, 2020. The copyright holder for this preprint (which was not certified by peer review) is the author/funder, who has granted bioRxiv a license to display the preprint in perpetuity. It is made available under aCC-BY-ND 4.0 International license.

cortical surface and recorded extracellular spiking activity with a silicon probe array in S1 of the lightly-anesthetized mouse (Fig. 7A). On "punctate sensory" trials, we presented 300 deg/s sawtooth whisker deflections, as described previously. On "punctate terminal" trials, we substituted the punctate sensory stimulus with brief optogenetic stimulation of TC terminals in the principal column. In both cases, we presented the punctate stimuli either in isolation (control trials) or embedded in a background sensory stimulus (adapted trials). We then considered the punctate sensory and punctate terminal responses of all single- and multi-units that responded significantly to the isolated punctate sensory stimulus (see Methods).

As shown above for awake (Fig. 1) and anesthetized (Fig. 4) mice, S1 sensory response grand PSTHs exhibited profound sensory adaptation (Fig. 7B, left). If this largely reflected synaptic depression, we would expect that punctate terminal stimulus responses would be similarly adapted by the background sensory stimulus. Instead, there was comparatively little evidence of adaptation in the grand PSTHs for punctate terminal trials (Fig. 7B, right). Importantly, this did not simply reflect an overwhelmingly strong LED stimulus; not only were evoked rates generally lower for LED responses than for punctate sensory responses across all neurons (Fig. 7B, C), but in exploring a variety of LED stimulus amplitudes and durations across experiments, we found that both relatively large- and small-amplitude LED-evoked PSTHs were at most only modestly adapted (not shown). This result also bore out in mean evoked rates: mean response rates for punctate sensory trials were profoundly adapted (Fig. 7C, left), while responses on punctate terminal trials were only slightly adapted (Fig. 7C, right), and the population median normalized adapted response was near 1 for punctate terminal trials, but significantly more negative for punctate sensory trials (Fig. 7D).

To investigate this more deeply, we repeated these anesthetized experiments while obtaining in vivo patch clamp recordings from neurons in S1 to inspect the subthreshold dynamics underlying these observations (Fig. 7E, left, see Methods). We recorded from four neurons that responded to both punctate sensory and terminal stimulation. While sensory- and light-evoked amplitudes varied across neurons (Fig. 7F, top), the adapting effects of the background stimulus on subthreshold sensory responses were generally not observed in terminal stimulation responses. Specifically, for punctate sensory responses, the across-trial mean amplitude significantly decreased for three cells, and the time to response peak significantly increased for all cells, (Fig. 7F, left, see Methods), consistent with the extracellular recordings (Fig. 7B, C). In contrast, almost none of these measures changed significantly for any of the cells' responses to terminal stimulation (Fig. 7F, right).

bioRxiv preprint doi: https://doi.org/10.1101/2020.10.08.331660; this version posted October 8, 2020. The copyright holder for this preprint (which was not certified by peer review) is the author/funder, who has granted bioRxiv a license to display the preprint in perpetuity. It is made available under aCC-BY-ND 4.0 International license.

While there are important caveats to consider when interpreting responses to optogenetic terminal stimulation (see Discussion), when taken together with the profound effects of adaptation on synchronous VPm spiking (Fig. 5G, H), and the lack of S1 adaptation under optogenetic elevation of baseline VPm rates (Fig. 6), these results suggest that rapid sensory adaptation of sensory-evoked firing rates in the awake mouse (Fig. 1) primarily reflects adaptation of thalamic sensory responses, with thalamocortical and intracortical synaptic adaptation playing a lesser role.

A model network identifies synchronous VPm spikes and robust feedforward inhibition as key mechanisms underlying S1 response adaptation

We observed profound adaptation of S1 sensory responses wakefulness (Fig. 1). Further, the degree of adaptation among RS (putative excitatory) cells was greater than would be predicted from that of FS cells (Fig. 1F – H) and upstream VPm cells (Fig. 5F). These observations, combined with the results of our anesthetized (Fig. 4) and optogenetic manipulation (Figs. 6, 7) experiments, suggest a particular mechanistic interpretation: cortical excitatory neurons are extremely sensitive to adaptive changes in synchronous VPm spiking, in part due to robust feedforward inhibition. As a final test of this assertion, we implemented a model thalamocortical network, and assessed its ability to reproduce profound, cell-type-specific adaptation.

We modeled a single S1 barrel as a clustered network of 800 excitatory and 100 inhibitory leaky integrate-and-fire neurons, subject to excitatory inputs from a model “VPm barreloid” (Fig. 8A). The barreloid was modeled as 40 independent trains of tonic and burst spikes, with spike times drawn from the empirical VPm probability distribution functions (PDFs, or normalized PSTHs). We selected cortical network and intrinsic neuronal parameters that mimicked measurements from previous studies, and then adjusted parameters slightly to ensure stable ongoing and evoked network activity (see Methods). We implemented differential thalamocortical (TC) connectivity, which consisted of three key components motivated by previous experimental work. First, inhibitory neurons had higher “TC convergence” (or proportion of VPm neurons that synapse onto each cortical neuron) than excitatories (0.75 vs. 0.5, (Bruno & Simons, 2002)). Second, the baseline and evoked firing rate of each VPm train was multiplied by a factor drawn from a skewed distribution (with mean of 1.0), and neurons with the highest rates synapsed exclusively onto inhibitory neurons ((Bruno & Simons, 2002), see Methods). Finally, TC synaptic latencies were on average 1 ms shorter for inhibitory neurons (Cruikshank et al., 2007; Kimura et al., 2010). With this architecture in place, we modeled 50 trials from each stimulus condition of interest.

We fine-tuned the model parameters to give qualitatively realistic peak rates for excitatory neurons when VPm spike times were drawn from the control (unadapted) empirical

bioRxiv preprint doi: https://doi.org/10.1101/2020.10.08.331660; this version posted October 8, 2020. The copyright holder for this preprint (which was not certified by peer review) is the author/funder, who has granted bioRxiv a license to display the preprint in perpetuity. It is made available under aCC-BY-ND 4.0 International license.

PSTHs for the 300 deg/s and 900 deg/s stimuli (Fig. 8B). Thus, the excitatory population was appropriately tuned to the rate and synchrony of thalamic firing. Next, we repeated the simulations using VPm spikes drawn from the adapted PSTHs (Fig. 8B, top, filled PSTH), and found that network excitatory neurons were in fact profoundly adapted, despite the only modest reduction in mean VPm rates (Fig. 8B, center). Further, excitatory neurons were generally more strongly adapted than inhibitory neurons in terms of mean evoked rate (Fig. 8B, C). Finally, as observed in experiment (Fig. 3D – G), synchronous spike counts were significantly reduced in the adapted condition for excitatory-excitatory (Fig. 8D, left) and inhibitory-inhibitory (Fig. 8D, right) pairs (see Methods), with a more drastic reduction for excitatory neurons. Thus, the mechanisms incorporated in this simple model were sufficient to qualitatively reproduce our key experimental results.

In these simulations, both the mean VPm rate (Fig. 8B, top) and VPm synchronous spiking (Fig. 8E, top) were reduced in the adapted condition. We next assessed the degree to which the loss in synchronous VPm spikes alone could explain cortical adaptation. To do this, we repeated the simulations while “manually” manipulating VPm spike times. Specifically, we first drew VPm spike times from the control PDFs, and for each spike that occurred within 5 ms of the PSTH peak time, we shifted the spike to a random higher latency (within approximately 20 ms of the peak) with 30% probability (see Methods). This had the effect of maintaining the mean evoked VPm rate, while reducing the number of near-coincident pairs of VPm spikes in the early response (Fig. 8E, bottom, “reduced synch“ condition). We found that this change alone – which only modestly affected the resulting VPm grand PSTH (Fig. 8F, top) – was sufficient to profoundly adapt mean excitatory evoked rates (Fig. 8F, center; 8G, top) and synchronous spike counts (Fig. 8H). In other words, with differential TC connectivity in place, a loss of synchronous VPm spiking was sufficient to reproduce the adapted cortical network response.

Finally, we asked whether robust feedforward inhibition – mediated by differential thalamocortical connectivity – contributed to the adaptation of network excitatory neurons. We modified the network slightly by setting identical TC convergence and TC synaptic latency values for excitatory and inhibitory neurons and eliminating rate-dependent TC connectivity (Fig. 8I). Inhibitory and excitatory neurons therefore had identical mean thalamocortical connection properties, though differences in intrinsic neuronal properties and dense excitatory-to-inhibitory connectivity still allowed for higher mean firing rates in the inhibitory population (see Methods). We then slightly reduced the mean TC synaptic weight to yield reasonable excitatory responses in the control condition (see Methods), before inspecting the responses to adapted VPm inputs. For this network, the mean evoked rates (Fig. 8J, top, K) and synchronous spike counts (Fig. 8L, left) for excitatory neurons were only modestly adapted compared to the model with differential TC connectivity, and the degree of adaptation more closely matched that of the inhibitory

bioRxiv preprint doi: https://doi.org/10.1101/2020.10.08.331660; this version posted October 8, 2020. The copyright holder for this preprint (which was not certified by peer review) is the author/funder, who has granted bioRxiv a license to display the preprint in perpetuity. It is made available under aCC-BY-ND 4.0 International license.

875 population (Fig. 8K, L, right). In other words, the excitatory population was less sensitive
876 to VPm adaptation when differential TC connectivity was removed. We used an additional
877 set of models to further assess the relative importance of each component of the
878 differential TC connectivity in the original model. While each component contributed, we
879 found that the degree of excitatory adaptation was most sensitive to differences in TC
880 synaptic latencies (not shown). This model thus demonstrates the role of robust
881 feedforward inhibition – reflecting differential TC connectivity – in shaping the adaptation
882 of cortical excitatory neurons.

883 Taken together, these simulations support our hypotheses that the profound adaptation
884 of cortical RS cells during wakefulness represents a loss of synchronous sensory-evoked
885 thalamic spikes, in conjunction with strong feedforward inhibition that is comparatively
886 robust to this decrease in feedforward thalamic drive.

887

bioRxiv preprint doi: https://doi.org/10.1101/2020.10.08.331660; this version posted October 8, 2020. The copyright holder for this preprint (which was not certified by peer review) is the author/funder, who has granted bioRxiv a license to display the preprint in perpetuity. It is made available under aCC-BY-ND 4.0 International license.

DISCUSSION

To determine the nature of rapid sensory adaptation and how it shapes sensory representations in primary sensory cortex during wakefulness, we recorded single-unit activity in S1 of the awake, head-fixed mouse while presenting punctate sensory stimuli either in isolation, or embedded in a persistent background stimulus. To elucidate the mechanistic basis of cortical adaptation, we identified putative excitatory and inhibitory cortical neurons and recorded from the lemniscal inputs to S1, while employing a battery of additional manipulations across the thalamocortical circuit. This approach allowed us to infer the contributions from thalamic adaptation, thalamocortical synaptic depression, and intracortical mechanisms. We further implemented a thalamocortical network model constrained by these observations to explore the relative roles of various candidate mechanisms at the level of cortex and thalamus.

Previous in vitro and anesthetized work has clearly demonstrated profound rapid sensory adaptation in sensory cortex (Cohen-Kashi Malina et al., 2013; Ganmor et al., 2010; Heiss et al., 2008; Kheradpezhouh et al., 2017; Ollerenshaw et al., 2014; Wang et al., 2010; Zheng et al., 2015), which is thought to represent the net effects on the circuit of elevated firing rates. Yet because baseline cortical firing rates are elevated during wakefulness compared to the anesthetized state (Aasebø et al., 2017; Greenberg et al., 2008; Vizuete et al., 2012), it remains an open question whether any room is left for fine-tuning by the sensory environment (Castro-Alamancos, 2004). Here, we demonstrate that cortical sensory responses can indeed be profoundly adapted during wakefulness. While we did not directly test the perceptual implications, the adaptive decrease in theoretical stimulus detectability and synchronous firing of putative cortical excitatory neurons suggest that downstream targets of S1 will be substantially less driven in the adapted state, which in general predicts a decrease in perceived stimulus intensity and a loss in behavioral detectability. In the specific context of the rodent whisker system, our observations are consistent with previous behavioral work in rats, which demonstrated changes in perceptual reporting following repetitive whisker stimulation (Ollerenshaw et al., 2014; Waiblinger et al., 2015) and whisker self-motion (Ollerenshaw et al., 2012), which elevates thalamic (Urbain et al., 2015) and cortical (Yu et al., 2016, 2019) firing rates. In other words, this study supports previous in vitro and anesthetized work suggesting cortical response adaptation could underlie adaptive changes in behavior.

We next sought to identify the mechanistic basis for S1 response adaptation. One body of literature implicates synaptic depression (Castro-Alamancos & Oldford, 2002; Chung et al., 2002; Cruikshank et al., 2010; Gabernet et al., 2005), while our previous work points to adaptation of thalamic spike timing (Ollerenshaw et al., 2014; Wang et al., 2010; Whitmire et al., 2016b), but both viewpoints have originated largely from in vitro or anesthetized preparations. Our results here in the awake mouse support the latter view. First, adaptation profoundly reduced single-unit bursting and the rate of evoked

bioRxiv preprint doi: https://doi.org/10.1101/2020.10.08.331660; this version posted October 8, 2020. The copyright holder for this preprint (which was not certified by peer review) is the author/funder, who has granted bioRxiv a license to display the preprint in perpetuity. It is made available under aCC-BY-ND 4.0 International license.

synchronous spikes in VPm, which predicts attenuated cortical firing (Bruno & Sakmann, 2006; Ollerenshaw et al., 2014; Swadlow & Gusev, 2001; Wang et al., 2010). Further, optogenetic elevation of baseline VPm rates did not adapt S1 responses to sensory stimuli, and background sensory stimulation had little effect on S1 responses to direct TC terminal stimulation, Finally, our modeling demonstrated that modest reductions in synchronous VPm spiking predicted profound adaptation of downstream excitatory neurons, Taken together, these results therefore demonstrate for the first time in the awake animal the sensitivity of cortex to thalamic spike timing in the context of sensory adaptation, and suggest that synaptic depression contributes little to the observed S1 response attenuation.

This apparent lack of TC synaptic depression appears to contradict the results of previous anesthetized and in vitro studies (Castro-Alamancos & Oldford, 2002; Chung et al., 2002; Cruikshank et al., 2010; Gabernet et al., 2005). We believe, however, that this reflects a difference in the strength of adapting stimuli. Specifically, these previous studies used adapting trains of high-velocity, punctate sensory stimuli and/or electrical stimulation, whereas we employed a relatively low-amplitude white noise adapting stimulus, which in terms of total power (Zheng et al., 2015) is many times weaker than the adapting stimuli used in some previous studies (not shown). This almost certainly adapts the TC circuit to a lesser degree than punctate stimulus trains, which may explain the apparent contradiction with previous work. This likely also explains why we did not observe stronger adaptation of FS units, which has been shown to reflect stronger adaptation of TC synapses onto inhibitory neurons (Gabernet et al., 2005).

When interpreting the results of our optogenetic TC terminal stimulation experiments, it is important to consider possible confounds. For example, light-evoked TC synaptic activity may be unnaturally synchronous across synapses, which could potentially negate the effects of synaptic depression. While we cannot rule out this possibility, we note that the optogenetic stimulus evoked a broad range of firing rates across recording sessions (Fig. 7C), due in part to our use of a variety of pulse amplitudes and durations, as well as variability in responsiveness across animals. Yet even weak light-evoked S1 activity was not appreciably adapted by sensory white noise, suggesting the results cannot be explained by over-synchronization of TC synapses. The light may also have stimulated TC terminals emanating from VPm neurons (in the principal and/or adjacent barreloids) that were at most weakly responsive to sensory stimulation, meaning these synapses would remain dormant (and unadapted) during background sensory stimulation. Still, this is extremely unlikely to explain the nearly identical “control” and “adapted” LED responses we observed; this would require that the LED primarily stimulated TC synapses from non-responsive VPm neurons, with almost no contribution from the synapses of sensory-responsive neurons in either the control or adapted conditions. This is unlikely, as we only considered S1 units that were significantly responsive to the punctate sensory

bioRxiv preprint doi: https://doi.org/10.1101/2020.10.08.331660; this version posted October 8, 2020. The copyright holder for this preprint (which was not certified by peer review) is the author/funder, who has granted bioRxiv a license to display the preprint in perpetuity. It is made available under aCC-BY-ND 4.0 International license.

stimulus (and were therefore substantially innervated by sensory-responsive VPm neurons).

While thalamic response adaptation appeared necessary for S1 adaptation, it did not explain the differential adaptation of mean evoked rate, response latency, and evoked synchronous spike counts among RS and FS cells during wakefulness. In other words, RS and FS cells did not provide the same read-out of thalamic spiking. In contrast, RS rates were no more adapted than FS rates under isoflurane anesthesia, which has been shown to disproportionately weaken cortical inhibition (Haider et al., 2013; Taub et al., 2013). This suggested to us that feedforward inhibition contributed to the adaptation of RS cells during wakefulness. We explored this possibility with a network model, in which we implemented cell-type-specific TC connectivity motivated by previous experimental work (Bruno & Simons, 2002): cortical inhibitory neurons were more densely innervated by TC synapses, and VPm neurons with the highest rates synapsed exclusively onto inhibitory neurons, yielding a more excitable inhibitory population. We found that S1 response adaptation did largely reflect a loss of synchronous VPm spikes, but that the profound and differential adaptation of excitatory neurons also required cell-type-specific TC connectivity. Taken together, these experimental and modeling results suggest a thalamocortical circuit basis for the observed S1 adaptation, involving a profound loss of synchronous feedforward excitation, and only a modest decrease in dampening feedforward inhibition.

This adaptive shift in the feedforward E/I balance toward inhibition has implications for cortical function and perception beyond attenuation of response amplitudes and perceived stimulus intensities. For example, previous experimental work has demonstrated that the relative strength and/or timing of cortical excitation and inhibition contributes to the direction-selectivity (Wilent & Contreras, 2005) and receptive field properties (Bruno & Simons, 2002; Kyriazi & Simons, 1993; Ramirez et al., 2014) of excitatory neurons, maintains relatively low excitatory firing rates during bouts of whisking (Gutnisky et al., 2017; Yu et al., 2016), shapes the “window of integration” during which excitatory neurons integrate excitatory synaptic inputs and depolarize toward threshold (Gabernet et al., 2005; Wilent & Contreras, 2005), and generally serves to “dampen” thalamic-evoked spiking in the excitatory subnetwork (D. J. Pinto et al., 2003). Thalamocortical adaptation exists on a continuum (Wang et al., 2010; Zheng et al., 2015), and more moderate levels of adaptation than we imposed here may result in moderately attenuated excitatory firing that is sharpened in space and time by comparatively non-adapted inhibition, resulting in more faithful spatiotemporal cortical representations of complex sensory stimuli. Future experiments exploring a broader range of adapting stimulus strengths and using more complex single- and multi-whisker stimulation can explore these possibilities.

bioRxiv preprint doi: https://doi.org/10.1101/2020.10.08.331660; this version posted October 8, 2020. The copyright holder for this preprint (which was not certified by peer review) is the author/funder, who has granted bioRxiv a license to display the preprint in perpetuity. It is made available under aCC-BY-ND 4.0 International license.

In summary, these results show the profound nature of rapid sensory adaptation at the level of primary sensory cortex that likely reflects the emergence of neural correlates that underlie perceptual adaptation on this timescale. Further, they highlight the relative importance of thalamic gating in establishing cortical adaptation, through population timing control of thalamic drive and the differential engagement of the inhibitory cortical sub-population.

bioRxiv preprint doi: https://doi.org/10.1101/2020.10.08.331660; this version posted October 8, 2020. The copyright holder for this preprint (which was not certified by peer review) is the author/funder, who has granted bioRxiv a license to display the preprint in perpetuity. It is made available under aCC-BY-ND 4.0 International license.

References

Aasebø, I. E. J., Lepperød, M. E., Stavrinou, M., Nøkkevangen, S., Einevoll, G., Hafting, T., & Fyhn, M. (2017). Temporal Processing in the Visual Cortex of the Awake and Anesthetized Rat. *Eneuro*, *4*(4), ENEURO.0059-17.2017. https://doi.org/10.1523/ENEURO.0059-17.2017

Anstis, S., Verstraten, F. A. J., & Mather, G. (1998). The motion aftereffect. *Trends in Cognitive Sciences*, *2*(3), 111–117. https://doi.org/10.1016/S1364-6613(98)01142-5

Barlow, H. B. (1961). Possible Principles Underlying the Transformations of Sensory Messages. In W. A. Rosenblith (Ed.), *Sensory Communication* (pp. 217–234). The MIT Press. https://doi.org/10.7551/mitpress/9780262518420.003.0013

Barthó, P., Slézia, A., Mátyás, F., Faradzs-Zade, L., Ulbert, I., Harris, K. D., & Acsády, L. (2014). Ongoing network state controls the length of sleep spindles via inhibitory activity. *Neuron*, *82*(6), 1367–1379. https://doi.org/10.1016/j.neuron.2014.04.046

Bestelmeyer, P. E. G., Rouger, J., DeBruine, L. M., & Belin, P. (2010). Auditory adaptation in vocal affect perception. *Cognition*, *117*(2), 217–223. https://doi.org/10.1016/j.cognition.2010.08.008

Blakemore, C., & Campbell, F. W. (1969). On the existence of neurones in the human visual system selectively sensitive to the orientation and size of retinal images. *The Journal of Physiology*, *203*(1), 237–260. https://doi.org/10.1113/jphysiol.1969.sp008862

Blakemore, Colin, & Nachmias, J. (1971). The orientation specificity of two visual after-effects. *The Journal of Physiology*, *213*(1), 157–174. https://doi.org/10.1113/jphysiol.1971.sp009374

Brecht, M., & Sakmann, B. (2002). Whisker maps of neuronal subclasses of the rat ventral posterior medial thalamus, identified by whole-cell voltage recording and morphological reconstruction. *The Journal of Physiology*, 495–515. https://doi.org/10.1013/jphysiol.2001.012334

Bruno, R. M., & Sakmann, B. (2006). Cortex is driven by weak but synchronously active thalamocortical synapses. *Science (New York, N.Y.)*, *312*(5780), 1622–1627. https://doi.org/10.1126/science.1124593

Bruno, R. M., & Simons, D. J. (2002). Feedforward mechanisms of excitatory and inhibitory cortical receptive fields. *J Neurosci*, *22*(24), 10966–10975. https://doi.org/22/24/10966 [pii]

Bujan, A. F., Aertsen, A., Kumar, X. A., Kumar, A., & Kumar, X. A. (2015). Role of Input Correlations in Shaping the Variability and Noise Correlations of Evoked Activity in the Neocortex. *Journal of Neuroscience*, *35*(22), 8611–8625. https://doi.org/10.1523/JNEUROSCI.4536-14.2015

Castro-Alamancos, M. A. (2004). Absence of Rapid Sensory Adaptation in Neocortex during Information Processing States. *Neuron*, *41*(3), 455–464.

bioRxiv preprint doi: https://doi.org/10.1101/2020.10.08.331660; this version posted October 8, 2020. The copyright holder for this preprint (which was not certified by peer review) is the author/funder, who has granted bioRxiv a license to display the preprint in perpetuity. It is made available under aCC-BY-ND 4.0 International license.

https://doi.org/10.1016/S0896-6273(03)00853-5

Castro-Alamancos, M. A., & Oldford, E. (2002). Cortical sensory suppression during arousal is due to the activity-dependent depression of thalamocortical synapses. *The Journal of Physiology*, *541*(1), 319–331. https://doi.org/10.1113/jphysiol.2002.016857

Chung, S., Li, X., & Nelson, S. B. (2002). Short-term depression at thalamocortical synapses contributes to rapid adaptation of cortical sensory responses in vivo. *Neuron*, *34*(3), 437–446. https://doi.org/10.1016/S0896-6273(02)00659-1

Cohen-Kashi Malina, K., Jubran, M., Katz, Y., & Lampl, I. (2013). Imbalance between excitation and inhibition in the somatosensory cortex produces postadaptation facilitation. *The Journal of Neuroscience : The Official Journal of the Society for Neuroscience*, *33*(19), 8463–8471. https://doi.org/10.1523/JNEUROSCI.4845-12.2013

Cruikshank, S. J., Lewis, T. J., & Connors, B. W. (2007). Synaptic basis for intense thalamocortical activation of feedforward inhibitory cells in neocortex. *Nature Neuroscience*, *10*(4), 462–468. https://doi.org/10.1038/nn1861

Cruikshank, S. J., Urabe, H., Nurmikko, A. V., & Connors, B. W. (2010). Pathway-Specific Feedforward Circuits between Thalamus and Neocortex Revealed by Selective Optical Stimulation of Axons. *Neuron*, *65*(2), 230–245. https://doi.org/10.1016/j.neuron.2009.12.025

Erb, J., Henry, M. J., Eisner, F., & Obleser, J. (2013). The brain dynamics of rapid perceptual adaptation to adverse listening conditions. *Journal of Neuroscience*, *33*(26), 10688–10697. https://doi.org/10.1523/JNEUROSCI.4596-12.2013

Gabernet, L., Jadhav, S. P., Feldman, D. E., Carandini, M., & Scanziani, M. (2005). Somatosensory integration controlled by dynamic thalamocortical feed-forward inhibition. *Neuron*, *48*(2), 315–327. https://doi.org/10.1016/j.neuron.2005.09.022

Ganmor, E., Katz, Y., & Lampl, I. (2010). Intensity-dependent adaptation of cortical and thalamic neurons is controlled by brainstem circuits of the sensory pathway. *Neuron*, *66*(2), 273–286. https://doi.org/10.1016/j.neuron.2010.03.032

Gentet, L. J., Avermann, M., Matyas, F., Staiger, J. F., & Petersen, C. C. H. H. (2010). Membrane potential dynamics of GABAergic neurons in the barrel cortex of behaving mice. *Neuron*, *65*(3), 422–435. https://doi.org/10.1016/j.neuron.2010.01.006

Ghodrati, M., Zavitz, E., Rosa, M. G. P., & Price, N. S. C. (2019). Contrast and luminance adaptation alter neuronal coding and perception of stimulus orientation. *Nature Communications*, *10*(1). https://doi.org/10.1038/s41467-019-08894-8

Greenberg, D. S., Houweling, A. R., & Kerr, J. N. D. (2008). Population imaging of ongoing neuronal activity in the visual cortex of awake rats. *Nature Neuroscience*, *11*(7), 749–751. https://doi.org/10.1038/nn.2140

Gutnisky, D. A., Yu, J., Hires, S. A., To, M. S., Bale, M. R., Svoboda, K., & Golomb, D.

bioRxiv preprint doi: https://doi.org/10.1101/2020.10.08.331660; this version posted October 8, 2020. The copyright holder for this preprint (which was not certified by peer review) is the author/funder, who has granted bioRxiv a license to display the preprint in perpetuity. It is made available under aCC-BY-ND 4.0 International license.

(2017). Mechanisms underlying a thalamocortical transformation during active tactile sensation. In *PLoS Computational Biology* (Vol. 13, Issue 6). https://doi.org/10.1371/journal.pcbi.1005576

Haider, B., Häusser, M., & Carandini, M. (2013). Inhibition dominates sensory responses in the awake cortex. *Nature*, *493*(7430), 97–102. https://doi.org/10.1038/nature11665

Hartings, J. A., Temereanca, S., & Simons, D. J. (2003). Processing of Periodic Whisker Deflections by Neurons in the Ventroposterior Medial and Thalamic Reticular Nuclei. *Journal of Neurophysiology*, *90*(5), 3087–3094. https://doi.org/10.1152/jn.00469.2003

Heiss, J. E., Katz, Y., Ganmor, E., & Lampl, I. (2008). Shift in the Balance between Excitation and Inhibition during Sensory Adaptation of S1 Neurons. *The Journal of Neuroscience : The Official Journal of the Society for Neuroscience*, *28*(49), 13320–13330. https://doi.org/10.1523/JNEUROSCI.2646-08.2008

Jadhav, S. P., & Feldman, D. E. (2010). Texture coding in the whisker system. *Current Opinion in Neurobiology*, *20*(3), 313–318. https://doi.org/10.1016/j.conb.2010.02.014

Jadhav, S. P., Wolfe, J., & Feldman, D. E. (2009). *Sparse temporal coding of elementary tactile features during active whisker sensation*. *12*(6). https://doi.org/10.1038/nn.2328

Khatri, V., Hartings, J. A., & Simons, D. J. (2004). Adaptation in thalamic barreloid and cortical barrel neurons to periodic whisker deflections varying in frequency and velocity. *Journal of Neurophysiology*, *92*(6), 3244–3254. https://doi.org/10.1152/jn.00257.2004

Kheradpezhouh, E., Adibi, M., & Arabzadeh, E. (2017). Response dynamics of rat barrel cortex neurons to repeated sensory stimulation. *Scientific Reports*, *7*(1), 1–10. https://doi.org/10.1038/s41598-017-11477-6

Kimura, F., Itami, C., Ikezoe, K., Tamura, H., Fujita, I., Yanagawa, Y., Obata, K., & Ohshima, M. (2010). Fast activation of feedforward inhibitory neurons from thalamic input and its relevance to the regulation of spike sequences in the barrel cortex. *Journal of Physiology*, *588*(15), 2769–2787. https://doi.org/10.1113/jphysiol.2010.188177

Kodandaramaiah, S. B., Holst, G. L., Wickersham, I. R., Singer, A. C., Franzesi, G. T., McKinnon, M. L., Forest, C. R., & Boyden, E. S. (2016). Assembly and operation of the autopatcher for automated intracellular neural recording in vivo. *Nature Protocols*, *11*(4), 634–654. https://doi.org/10.1038/nprot.2016.007

Kyriazi, H., & Simons, D. (1993). Thalamocortical response transformations in simulated whisker barrels. *The Journal of Neuroscience*, *13*(4), 1601–1615. https://doi.org/10.1523/JNEUROSCI.13-04-01601.1993

Litwin-Kumar, A., & Doiron, B. (2012). Slow dynamics and high variability in balanced

bioRxiv preprint doi: https://doi.org/10.1101/2020.10.08.331660; this version posted October 8, 2020. The copyright holder for this preprint (which was not certified by peer review) is the author/funder, who has granted bioRxiv a license to display the preprint in perpetuity. It is made available under aCC-BY-ND 4.0 International license.

cortical networks with clustered connections. *Nature Neuroscience*, *15*(11), 1498–1505. https://doi.org/10.1038/nn.3220

Liu, C., Foffani, G., Scaglione, A., Aguilar, J., & Moxon, K. A. (2017). Adaptation of thalamic neurons provides information about the spatiotemporal context of stimulus history. *The Journal of Neuroscience*, 0637–17. https://doi.org/10.1523/JNEUROSCI.0637-17.2017

Manita, S., Suzuki, T., Homma, C., Matsumoto, T., Odagawa, M., Yamada, K., Ota, K., Matsubara, C., Inutsuka, A., Sato, M., Ohkura, M., Yamanaka, A., Yanagawa, Y., Nakai, J., Hayashi, Y., Larkum, M. E., & Murayama, M. (2015). A Top-Down Cortical Circuit for Accurate Sensory Perception. *Neuron*, *86*(5), 1304–1316. https://doi.org/10.1016/j.neuron.2015.05.006

McGinley, M. J. M. M. J., David, S. S. V. S. S. V. S., & McCormick, D. A. (2015). Cortical Membrane Potential Signature of Optimal States for Sensory Signal Detection. *Neuron*, *87*(1), 179–192. https://doi.org/10.1016/j.neuron.2015.05.038

Mcginley, M. J., Vinck, M., Reimer, J., Batista-Brito, R., Zagha, E., Cadwell, C. R., Tolias, A. S., Cardin, J. A., & Mccormick, D. A. (2015). Waking State: Rapid Variations Modulate Neural and Behavioral Responses. *Neuron*, *87*(6), 1143–1161. https://doi.org/10.1016/j.neuron.2015.09.012

Musall, S., Behrens, W. Von Der, Mayrhofer, J. M., Weber, B., Helmchen, F., Haiss, F., Von Der Behrens, W., Mayrhofer, J. M., Weber, B., Helmchen, F., Haiss, F., Behrens, W. Von Der, Mayrhofer, J. M., Weber, B., Helmchen, F., & Haiss, F. (2014). Tactile frequency discrimination is enhanced by circumventing neocortical adaptation. *Nature Neuroscience*, *17*(11), 1567–1573. https://doi.org/10.1038/nn.3821

Ollerenshaw, D. R., Bari, B. a, Millard, D. C., Orr, L. E., Wang, Q., & Stanley, G. B. (2012). Detection of tactile inputs in the rat vibrissa pathway. *Journal of Neurophysiology*, *108*(2), 479–490. https://doi.org/10.1152/jn.00004.2012

Ollerenshaw, D. R., Zheng, H. J. V., Millard, D. C., Wang, Q., & Stanley, G. B. (2014). The Adaptive Trade-Off between Detection and Discrimination in Cortical Representations and Behavior. *Neuron*, *81*(5), 1152–1164. https://doi.org/10.1016/j.neuron.2014.01.025

Pinto, D. J. D., Brumberg, J. C. J., & Simons, D. J. D. J. (2000). Circuit dynamics and coding strategies in rodent somatosensory cortex. *Journal of Neurophysiology*, *83*(3), 1158–1166. https://doi.org/10.1152/jn.2000.83.3.1158

Pinto, D. J., Hartings, J. A., Brumberg, J. C., & Simons, D. J. (2003). Cortical damping: Analysis of thalamocortical response transformations in rodent barrel cortex. *Cerebral Cortex*, *13*(1), 33–44. https://doi.org/10.1093/cercor/13.1.33

Ramirez, A., Pnevmatikakis, E. A., Merel, J., Paninski, L., Miller, K. D., & Bruno, R. M. (2014). Spatiotemporal receptive fields of barrel cortex revealed by reverse correlation of synaptic input. *Nat Neurosci*, *17*(6), 866–875. https://doi.org/10.1038/nn.3720

bioRxiv preprint doi: https://doi.org/10.1101/2020.10.08.331660; this version posted October 8, 2020. The copyright holder for this preprint (which was not certified by peer review) is the author/funder, who has granted bioRxiv a license to display the preprint in perpetuity. It is made available under aCC-BY-ND 4.0 International license.

Reimer, J., Froudarakis, E., Cadwell, C. R., Yatsenko, D., Denfield, G. H., & Tolias, A. S. (2014). Pupil Fluctuations Track Fast Switching of Cortical States during Quiet Wakefulness. *Neuron*, *84*(2), 355–362. https://doi.org/10.1016/j.neuron.2014.09.033

Reimer, J., Mcginley, M. J., Liu, Y., Rodenkirch, C., Wang, Q., McCormick, D. A., & Tolias, A. S. (2016). Pupil fluctuations track rapid changes in adrenergic and cholinergic activity in cortex. *Nature Communications*, *7*(May), 1–7. https://doi.org/10.1038/ncomms13289

Ritt, J. T., Andermann, M. L., & Moore, C. I. (2008). Embodied Information Processing: Vibrissa Mechanics and Texture Features Shape Micromotions in Actively Sensing Rats. *Neuron*, *57*(4), 599–613. https://doi.org/10.1016/j.neuron.2007.12.024

Safaai, H., von Heimendahl, M., Sorando, J. M., Diamond, M. E., & Maravall, M. (2013). Coordinated Population Activity Underlying Texture Discrimination in Rat Barrel Cortex. *Journal of Neuroscience*, *33*(13), 5843–5855. https://doi.org/10.1523/JNEUROSCI.3486-12.2013

Sederberg, A., Pala, A., Zheng, H., He, B. J., & Stanley, G. B. (2018). *State-aware detection of sensory stimuli in the cortex of the awake mouse*.

Sermet, B. S., Truschow, P., Feyerabend, M., Mayrhofer, J. M., Oram, T. B., Yizhar, O., Staiger, J. F., & Petersen, C. C. H. (2019). Pathway-, layer-and cell-type-specific thalamic input to mouse barrel cortex. *ELife*, *8*, 1–28. https://doi.org/10.7554/eLife.52665

Sherman, S. M. (2001). A wake-up call from the thalamus. *Nature Neuroscience*, *4*(4), 344–346. https://doi.org/10.1038/85973

Smith, M. W., & Faulkner, A. (2006). Perceptual adaptation by normally hearing listeners to a simulated “hole” in hearing. *The Journal of the Acoustical Society of America*, *120*(6), 4019–4030. https://doi.org/10.1121/1.2359235

Stoy, W. M., Yang, B., Kight, A., Wright, N. C., Borden, P. Y., Stanley, G. B., & Forest, C. R. (2020). Compensation of physiological motion enables high-yield whole-cell recording in vivo. *Biorxiv*. https://doi.org/https://doi.org/10.1101/2020.06.09.143008v1

Suzuki, M., & Larkum, M. E. (2020). General Anesthesia Decouples Cortical Pyramidal Neurons. *Cell*, *180*(4), 666-676.e13. https://doi.org/10.1016/j.cell.2020.01.024

Swadlow, H. A. (2002). Thalamocortical control of feed-forward inhibition in awake somatosensory “barrel” cortex. *Philosophical Transactions of the Royal Society B: Biological Sciences*, *357*(1428), 1717–1727. https://doi.org/10.1098/rstb.2002.1156

Swadlow, H. A., & Gusev, A. G. (2001). The impact of “bursting” thalamic impulses at a neocortical synapse. *Nature Neuroscience*, *4*(4), 402–408. https://doi.org/10.1038/86054

Tannan, V., Simons, S., Dennis, R. G., & Tommerdahl, M. (2007). Effects of adaptation on the capacity to differentiate simultaneously delivered dual-site vibrotactile

bioRxiv preprint doi: https://doi.org/10.1101/2020.10.08.331660; this version posted October 8, 2020. The copyright holder for this preprint (which was not certified by peer review) is the author/funder, who has granted bioRxiv a license to display the preprint in perpetuity. It is made available under aCC-BY-ND 4.0 International license.

stimuli. *Brain Research*, *1186*(1), 164–170. https://doi.org/10.1016/j.brainres.2007.10.024

Taub, A. H., Katz, Y., & Lampl, I. (2013). Cortical Balance of Excitation and Inhibition Is Regulated by the Rate of Synaptic Activity. *Journal of Neuroscience*, *33*(36), 14359–14368. https://doi.org/10.1523/JNEUROSCI.1748-13.2013

Urbain, N., Salin, P. A., Libourel, P. A., Comte, J. C., Gentet, L. J., & Petersen, C. C. H. (2015). Whisking-Related Changes in Neuronal Firing and Membrane Potential Dynamics in the Somatosensory Thalamus of Awake Mice. *Cell Reports*, *13*(4), 647–656. https://doi.org/10.1016/j.celrep.2015.09.029

Vizuete, J. A., Pillay, S., Diba, K., Ropella, K. M., & Hudetz, A. G. (2012). Monosynaptic functional connectivity in cerebral cortex during wakefulness and under graded levels of anesthesia. *Frontiers in Integrative Neuroscience*, *6*(SEPTEMBER), 1–11. https://doi.org/10.3389/fnint.2012.00090

Waiblinger, C., Brugger, D., Whitmire, C. J., Stanley, G. B., & Schwarz, C. (2015). Support for the slip hypothesis from whisker-related tactile perception of rats in a noisy environment. *Frontiers in Integrative Neuroscience*, *9*(October), e53. https://doi.org/10.3389/fnint.2015.00053

Wang, Q., Webber, R. M., & Stanley, G. B. (2010). Thalamic synchrony and the adaptive gating of information flow to cortex. *Nature Neuroscience*, *13*(12), 1534–1541. https://doi.org/10.1038/nn.2670

Whitmire, C. J., Waiblinger, C., Schwarz, C., & Stanley, G. B. (2016a). Information Coding through Adaptive Gating of Article Information Coding through Adaptive Gating of Synchronized Thalamic Bursting. *CellReports*, 1–13. https://doi.org/10.1016/j.celrep.2015.12.068

Whitmire, C. J., Waiblinger, C., Schwarz, C., & Stanley, G. B. (2016b). Information Coding through Adaptive Gating of Synchronized Thalamic Bursting. *Cell Reports*, *14*(4), 795–807. https://doi.org/10.1016/j.celrep.2015.12.068

Wilent, W. B., & Contreras, D. (2005). Dynamics of excitation and inhibition underlying stimulus selectivity in rat somatosensory cortex. *Nature Neuroscience*, *8*(10), 1364–1370. https://doi.org/10.1038/nn1545

Wolfe, J., Hill, D. N., Pahlavan, S., Drew, P. J., Kleinfeld, D., & Feldman, D. E. (2008). Texture coding in the rat whisker system: Slip-stick versus differential resonance. *PLoS Biology*, *6*(8), 1661–1677. https://doi.org/10.1371/journal.pbio.0060215

Wright, N. C., Hoseini, M. S., & Wessel, R. (2017). Adaptation modulates correlated subthreshold response variability in visual cortex. *Journal of Neurophysiology*, *118*(2), 1257–1269. https://doi.org/10.1152/jn.00124.2017

Wright, N. C., Hoseini, M. S., Yasar, T. B., & Wessel, R. (2017). Coupling of synaptic inputs to local cortical activity differs among neurons and adapts after stimulus onset. *Journal of Neurophysiology*, *118*(6), 3345–3359. https://doi.org/10.1152/jn.00398.2017

bioRxiv preprint doi: https://doi.org/10.1101/2020.10.08.331660; this version posted October 8, 2020. The copyright holder for this preprint (which was not certified by peer review) is the author/funder, who has granted bioRxiv a license to display the preprint in perpetuity. It is made available under aCC-BY-ND 4.0 International license.

1252 Yu, J., Gutnisky, D. A., Hires, S. A., & Svoboda, K. (2016). Layer 4 fast-spiking
1253 interneurons filter thalamocortical signals during active somatosensation. *Nature*
1254 *Neuroscience*, *19*(12), 1647–1657. https://doi.org/10.1038/nn.4412

1255 Yu, J., Hu, H., Agmon, A., Yu, J., Hu, H., Agmon, A., & Svoboda, K. (2019). Recruitment
1256 of GABAergic Interneurons in the Barrel Cortex during Active Tactile Behavior
1257 Article Recruitment of GABAergic Interneurons in the Barrel Cortex during Active
1258 Tactile Behavior. *Neuron*, 1–16. https://doi.org/10.1016/j.neuron.2019.07.027

1259 Zheng, H. J. V., Wang, Q., & Stanley, G. B. (2015). Adaptive shaping of cortical
1260 response selectivity in the vibrissa pathway. *Journal of Neurophysiology*, *113*(10),
1261 3850–3865. https://doi.org/10.1152/jn.00978.2014

1262 Zuo, Y., Safaai, H., Notaro, G., Mazzoni, A., Panzeri, S., & Diamond, M. E. (2015).
1263 Complementary Contributions of Spike Timing and Spike Rate to Perceptual
1264 Decisions in Rat S1 and S2 Cortex. *Current Biology*, *25*(3), 357–363.
1265 https://doi.org/10.1016/j.cub.2014.11.065

1266

1267

1268

bioRxiv preprint doi: https://doi.org/10.1101/2020.10.08.331660; this version posted October 8, 2020. The copyright holder for this preprint (which was not certified by peer review) is the author/funder, who has granted bioRxiv a license to display the preprint in perpetuity. It is made available under aCC-BY-ND 4.0 International license.

Figure Captions

Figure 1. S1 exhibits sensory adaptation during wakefulness, and regular-spiking neurons are more profoundly adapted than fast-spiking neurons. A. Experimental setup. We recorded in S1 of the awake, head-fixed mouse while presenting precise single-whisker stimulation. "Sawtooth" punctate whisker deflections were delivered either in isolation (control condition) or embedded in sensory white noise (adapted condition). B. Top: Grand mean +/- SEM waveforms for all well-isolated fast-spiking (FS, blue, N = 95) and regular-spiking (RS, red, N = 119) significantly responsive single-units recorded in S1 of awake mice (see Methods). Bottom: distribution of mean waveform widths (time from trough to subsequent peak) for all units, with color denoting RS and FS designation. C. Summed spiking activity of regular-spiking (RS, putative excitatory) and fast-spiking (FS, putative inhibitory) from one example recording session. Each row indicates spike times of all simultaneously-recorded RS (red) and FS (blue) neurons on a single trial. D. Grand-average mean (+/- SEM) rates for spontaneous activity (i.e., no sensory stimulation) and during the presentation of sensory white noise (with *** indicating $p < 0.001$, Wilcoxon signed-rank test). RS: spontaneous rate = 6.0 +/- 0.59 Hz, white-noise-evoked rate = 8.11 +/- 0.74 Hz, mean +/- SEM, 35.1% increase, $p = 6.17 \times 10^{-8}$, Wilcoxon signed-rank test, N = 119 units from 19 recording sessions, FS: spontaneous rate = 12.28 +/- 1.22 Hz, white-noise-evoked rate = 26.1 +/- 2.73 Hz, mean +/- SEM, 112.6% increase, $p = 2.41 \times 10^{-16}$, Wilcoxon signed-rank test, N = 95 units from 19 sessions. E. Grand PSTHs for all responsive RS (top, N = 119) and FS (bottom, N = 95) units, for two punctate stimulus velocities. F. Across-neuron mean (+/- SEM) firing rates for all responsive neurons, for 300 deg/s (left) and 900 deg/s (right) punctate stimuli (*: $0.01 \leq p < 0.05$; ***: $p < 0.001$, Wilcoxon singed-rank test). RS 300 deg/s mean +/- SEM control: 17.08 +/- 1.02, adapted: 11.36 +/- 1.01, 33.5% decrease, $p = 1.03 \times 10^{-15}$, Wilcoxon signed-rank test, N = 119 units; 900 control: 17.19 +/- 1.25 Hz, adapted: 9.92 +/- 1.08 Hz, 42.3% decrease, $p = 1.47 \times 10^{-8}$, N = 49 units from 8 sessions; FS: 300 deg/s control: 41.72 +/- 3.85 Hz, adapted: 34.1 +/- 3.39 Hz, 18.3% decrease $p = 2.90 \times 10^{-8}$, N = 95 units from 19 sessions; 900 deg/s control: 42.88 +/- 5.61 Hz, adapted: 40.03 +/- 6.43 Hz, 6.6% decrease $p = 0.19$, N = 29 units from 8 sessions. G. Population median (+/- SEM)

bioRxiv preprint doi: https://doi.org/10.1101/2020.10.08.331660; this version posted October 8, 2020. The copyright holder for this preprint (which was not certified by peer review) is the author/funder, who has granted bioRxiv a license to display the preprint in perpetuity. It is made available under aCC-BY-ND 4.0 International license.

normalized adapted responses for all responsive RS (red) and FS (blue) neurons (see Methods; ***: $p < 0.001$, Kruskal-Wallis test). RS 300 deg/s median normed adapted response = 0.61, FS median normed adapted response = 0.77, $p = 3.85 \times 10^{-5}$, Kruskal-Wallis test; 900 deg/s RS median normed adapted response = 0.47, FS median normed adapted response = 0.87, $p = 1.13 \times 10^{-4}$. H. Population median normalized adapted responses (+/- SEM) by binned cortical depth (see Methods).

Figure 2. Adaptation reduces the theoretical detectability of punctate sensory stimuli. A. Schematic overview of signal detection theory. Theoretical detectability depends on the degree to which the distributions for "stimulus" (i.e., sensory response amplitudes, green) and "no-stimulus" (i.e., ongoing activity amplitudes, gray) overlap. B. Generation of ongoing and evoked population activity distributions for one example session (see Methods). For this session (representative of the average), adaptation decreased the population response amplitude, increasing the overlap of the ongoing and evoked distributions (right). C. Receiver operator characteristic (ROC) curves for example session in (B), for the control (darker line) and adapted (lighter line) conditions, and associated area under ROC curve (AUROC) values. D. Theoretical detectability (AUROC) vs. stimulus condition for all awake sessions (***: $p < 0.001$, Wilcoxon signed-rank test). Control AUROC = 0.91 +/- 0.02, adapted AUROC = 0.76 +/- 0.02, $p = 1.8 \times 10^{-4}$, Wilcoxon signed-rank test, N = 19 recording sessions.

Figure 3. Adaptation increases response latency and reduces pairwise synchronous spiking in S1. A. Calculation of response onset properties for example RS unit. Spike trains for each trial were convolved with a Gaussian kernel and summed across trials, resulting in a convolved spike count ($\tilde{s}$), from which we calculated response onset times (T_{onset}) and max rate of change in $\tilde{s}$ immediately after T_{onset} (max $d\tilde{s}/dt$, see Methods). B. Grand mean onset times for RS (red) and FS (blue) neurons, for control and adapted responses to 300 deg/s stimulus (***: $p < 0.001$; single gray bar: $p \geq 0.05$, Wilcoxon signed-rank test, control vs. adapted). 300 deg/s RS mean +/ SEM control: T_{onset} = 8.81 +/- 0.53 ms, adapted: 15.31 +/- 0.98 ms, 73.9% increase, $p = 3.11 \times 10^{-11}$,

bioRxiv preprint doi: https://doi.org/10.1101/2020.10.08.331660; this version posted October 8, 2020. The copyright holder for this preprint (which was not certified by peer review) is the author/funder, who has granted bioRxiv a license to display the preprint in perpetuity. It is made available under aCC-BY-ND 4.0 International license.

Wilcoxon signed-rank test, N = 119 units; FS control: T_{onset} = 6.69 +/- 0.37 ms, adapted: 8.95 +/- 0.7 ms, 33.9% increase, p = 8.11 x 10^{-7}, N = 95 units, Fig. 3B; 900 deg/s RS control: T_{onset} = 7.89 +/- 0.49 ms, adapted: 11.36 +/- 1.07 ms, 43.9% increase, p = 1.70 x 10^{-5}, N = 49 units; FS control: T_{onset} = 5.67 +/- 0.29 ms, adapted: 6.27 +/- 0.63 ms, p = 0.27. C. Illustration of synchronous spike-count calculation. The grand cross-correlogram (CCG) was constructed using all valid pairs of simultaneously-recorded S1 units, then scaled by the number of contributing pairs, and shuffle-corrected (see Methods). The synchronous spike count was the number of spikes in a +/- 7.5 ms window around zero lag. D. Grand RS-RS CCGs for responses to 300 deg/s stimulus, for the control (dark red) and adapted (light red) conditions. Bands indicate 99.9% confidence intervals (from re-sampling spikes with replacement, see Methods). E. Synchronous AP counts for control and adapted responses, calculated from RS-RS grand CCGs in (D). Error bars indicate 99.9% confidence intervals (from re-sampling spikes with replacement, see Methods). RS-RS pairs: 300 deg/s mean +/- 99.9% confidence interval control: synch AP count = 65.93 +/- 3.31 spikes/pair, adapted: 22.14 +/- 2.11 spikes/pair, 66.4% decrease, p < 0.001, N = 189 valid pairs from 17 sessions; 900 deg/s control: 135.64 +/- 7.53 spikes/pair; adapted: 25.67 +/- 3.65 spikes/pair, 81.1% decrease, p < 0.001, N = 55 valid pairs from 6 sessions. F and G. Same as (D) and (E), but for valid FS-FS pairs. FS-FS pairs: 300 deg/s control: 253.47 +/- 8.64 spikes/pair, adapted: 173.73 +/- 7.56 spikes/pair, 31.5% decrease, p < 0.001, N = 118 valid pairs from 17 sessions; 900 deg/s control: 597.33 +/- 23.79 spikes/pair; adapted: 379.8 +/- 19.6 spikes/pair, 36.4% decrease, p < 0.001, N = 33 valid pairs from 6 sessions, see Methods for definition of “valid pairs”.

Figure 4. S1 sensory responses are also adapted under anesthesia, but RS cells are not differentially adapted. A. Experimental setup. S1 sensory responses were recorded in mice lightly-anesthetized with isoflurane (see Methods). B. Summed spiking activity of regular-spiking (RS, putative excitatory) and fast-spiking (FS, putative inhibitory) from one example recording session. Each row indicates spike times of all simultaneously-recorded RS (red) and FS (blue) neurons on a single trial. C. Grand-

bioRxiv preprint doi: https://doi.org/10.1101/2020.10.08.331660; this version posted October 8, 2020. The copyright holder for this preprint (which was not certified by peer review) is the author/funder, who has granted bioRxiv a license to display the preprint in perpetuity. It is made available under aCC-BY-ND 4.0 International license.

average mean (+/- SEM) rates for spontaneous activity (i.e., no sensory stimulation) and during the presentation of sensory white noise (with *** indicating $p < 0.001$, Wilcoxon signed-rank test). RS: spontaneous rate = 2.31 +/- 0.37 Hz, white-noise-evoked rate = 3.77 +/- 0.4 Hz, mean +/- SEM, 63.4% increase, $p = 2.44 \times 10^{-7}$, Wilcoxon signed-rank test, N = 46 units from 14 sessions, Fig. 2C; FS: spontaneous rate = 0.83 +/- 0.26 Hz, white-noise-evoked rate = 6.29 +/- 0.92 Hz, mean +/- SEM, 657% increase, $p = 5.60 \times 10^{-5}$, N = 21 units from 14 sessions. D. Sensory response grand PSTHs for all responsive RS (left, N = 46) and FS (right, N = 21) units recorded under anesthesia, for 300 deg/s punctate stimulus velocity. Grand mean (+/- SEM) rates for cells contributing to PSTHs in (D). RS mean +/- SEM control: 12.27 +/- 0.88 Hz, adapted: 7.75 +/- 1.01, 36.8% decrease, $p = 9.82 \times 10^{-5}$; FS control: 18.61 +/- 2.19 Hz, adapted: 11.94 +/- 2.61, 35.8% decrease, $p = 0.001$. F. Population median (+/- SEM) normalized adapted responses for all responsive RS (red) and FS (blue) neurons (see Methods). RS 300 deg/s median normed adapted response = 0.54, FS median normed adapted response = 0.57, $p = 0.91$, Kruskal-Wallis test.

Figure 5. Adaptation reduces tonic and burst firing rates, and synchronous spike counts, in VPm sensory responses. A. Experimental setup. We recorded extracellular spiking in VPm of the awake mouse, primarily using high-density silicon probes (see Methods). B. Top: summed spiking activity of all well-isolated, responsive, putative VPm units (see Methods) from one example recording session. Each row indicates spike times of all such simultaneously-recorded units on a single trial. C. Grand-average mean (+/- SEM) rates for spontaneous activity (i.e., no sensory stimulation) and during the presentation of sensory white noise (with *** indicating $p < 0.001$, Wilcoxon signed-rank test). Mean +/- SEM spontaneous: rate = 10.5 +/- 1.29 Hz, white noise: rate = 15.58 +/- 2.5 Hz, 48.4% increase $p = 9.63 \times 10^{-4}$, Wilcoxon signed-rank test, N = 30 units from 9 recording sessions. D. Criteria for classification of putative tonic (black) and burst (red) VPm spikes. E. Grand PSTHs for tonic (black) and burst (red) spikes from all putative VPm neurons, for 300 deg/s punctate stimulus. F. Across-neuron mean (+/- SEM) firing rates for all putative VPm neurons (**: $0.001 \leq p < 0.01$; ***: $p < 0.001$, Wilcoxon singed-

bioRxiv preprint doi: https://doi.org/10.1101/2020.10.08.331660; this version posted October 8, 2020. The copyright holder for this preprint (which was not certified by peer review) is the author/funder, who has granted bioRxiv a license to display the preprint in perpetuity. It is made available under aCC-BY-ND 4.0 International license.

rank test). tonic 300 deg/s mean +/- SEM rate control: 30.2 +/- 3.41 Hz, adapted: 24.32 +/- 2.92 Hz, 19.5% decrease, N = 30 units, p = 0.002, Wilcoxon signed-rank test; 900 control: 29.98 +/- 3.47 Hz, adapted: 26.87 +/- 3.18 Hz, N = 16 units, p = 0.22; burst: 300 deg/s control: 3.79 +/- 1.08, adapted: 1.37 +/- 0.73 Hz, 64.0% decrease, $p = 6.21 \times 10^{-4}$; 900 deg/s control: 5.75 +/- 3.13 Hz, adapted: 2.02 +/- 0.88, 64.9% decrease, $p = 4.6 \times 10^{-3}$. G. Grand shuffle-corrected cross-correlograms for all simultaneously-recorded putative VPm neurons, for the control (black) and adapted (gray) conditions. Bands indicate 99.9% confidence intervals (from re-sampling spikes with replacement, see Methods). H. Mean synchronous AP counts, calculated from CCGs in (G), with error bars indicating 99.99% confidence intervals (***: $p < 0.001$, re-sampling spikes with replacement). 300 deg/s mean +/- 99.9% confidence interval control: synch AP count = 42.96 +/- 8.9 spikes/pair, adapted: 16.6 +/- 6.19 spikes/pair, 61.4% decrease, $p < 0.001$, N = 48 valid pairs from 7 sessions; 900 deg/s control: 54.1 +/- 10.43 spikes/pair; adapted: 31.51 +/- 9.24 spikes/pair, 41.7% decrease, $p < 0.001$, N = 37 valid pairs from 3 sessions, see Methods for definition of “valid pairs”

Figure 6. Optogenetic elevation of baseline VPm firing rate does not adapt S1 sensory responses. A. Experimental setup. We recorded extracellular spiking activity from topographically-aligned VPm barreloids and S1 barrels in awake, head-fixed, transgenic mice expressing Channelrhodopsin in VPm/VPl neurons (see Methods). B. Summed spiking activity of all well-isolated, responsive putative VPm (top) and S1 (bottom) units from one example recording session. Each row indicates spike times of all such simultaneously-recorded units in that brain region on a single trial. C. Grand mean (+/- SEM) firing rates for spontaneous activity (“spont”), and during presentation of the adapting sensory stimulus (“white noise”) and optogenetic depolarization of VPm (“LED”), for VPm (top) and S1 (bottom; *: $0.005 \leq p < 0.025$; **: $5 \times 10^{-4} \leq p < 5 \times 10^{-3}$; ***: $p < 5 \times 10^{-4}$). VPm mean +/- SEM rate spontaneous: 7.68 +/- 1.1 Hz, white noise: 11.05 +/- 1.99 Hz, LED: 14.27 +/- 2.81 Hz, 44.0% increase spont vs. white noise, p = 0.011, Wilcoxon signed-rank test, 85.9% increase spont vs. LED, p = 0.011, 29.2% increase white noise vs. LED, p = 0.91, N = 20 units from six sessions; S1 spontaneous: 8.87 +/- 0.82 Hz,

bioRxiv preprint doi: https://doi.org/10.1101/2020.10.08.331660; this version posted October 8, 2020. The copyright holder for this preprint (which was not certified by peer review) is the author/funder, who has granted bioRxiv a license to display the preprint in perpetuity. It is made available under aCC-BY-ND 4.0 International license.

white noise: 16.32 +/- 2.05 Hz, LED: 10.03 +/- 1.05 Hz, 87.7% increase spont vs. white noise, $p = 5.05 \times 10^{-10}$, 15.3% increase spont vs. LED, p = 0.11, spont vs. LED, 38.6% decrease white noise vs. LED, $p = 8.42 \times 10^{-5}$, N = 88 units from six sessions. D. Left: grand PSTHs for each stimulus condition, for VPm (top) and S1 (bottom). Right: Grand mean (+/- SEM) firing rates for each condition. Asterisks as in (C). S1 mean +/- SEM rate control: 27.33 +/- 2.61 Hz, adapted: 20.91 +/- 2.47 Hz, LED: 27.82 +/- 2.79 Hz, 23.5% decrease control vs. adapted, $p = 1.39 \times 10^{-9}$, 1.76% increase control vs. LED, p = 0.89, Wilcoxon signed-rank test; VPm control: 29.12 +/- 4.82 Hz, adapted: 19.07 +/- 3.1 Hz, LED: 36.44 +/- 5.35 Hz, 34.5% decrease control vs. adapted, p = 0.003, 25.16% increase control vs. LED, p = 0.06. E. Top: Grand VPm CCGs for each stimulus condition. Bands indicate 99.9% confidence intervals (re-sampling spikes with replacement (see Methods). Bottom: synchronous spike counts calculated from CCGs in (E, Top), for each stimulus condition. Error bars indicate 99.9% confidence intervals (re-sampling spikes with replacement (see Methods). Mean +/- 99.9% confidence interval synch AP count control: 47.14 +/- 11.0 spikes/pair, LED: 51.83 +/- 12.94 spikes/pair, adapted: 20.08 +/- 8.53 spikes/pair, $p \geq 0.05$ control vs. LED, $p < 0.001$ control vs. adapted, re-sampling spikes with replacement, N = 36 pairs from 19 units in five sessions.

Figure 7. S1 responses to direct optogenetic stimulation of TC terminals are not adapted by sensory white noise. A. Experimental setup for extracellular recordings. S1 spiking activity was recorded in mice lightly-anesthetized with isoflurane (see Methods). These transgenic mice expressed Channelrhodopsin in VPm cell bodies, axons, and thalamocortical (TC) axon terminals. An optic fiber positioned above the cortical surface was used to deliver punctate optogenetic stimulation to TC terminals on "punctate terminal" stimulation trials (see Methods). B. Grand PSTHs (using all sensory-responsive single- and multi-units, see Methods) for punctate sensory (black, left) and punctate terminal (blue, right) trials, for control (empty histogram) and adapted (filled histogram) conditions. C. Across-unit mean (+/- SEM) punctate-stimulus-evoked firing rates vs stimulus condition for all responsive single- and multi-units, for punctate sensory (black, left) and punctate terminal (blue, right) stimuli. (***: $p < 0.001$, Wilcoxon singed-

bioRxiv preprint doi: https://doi.org/10.1101/2020.10.08.331660; this version posted October 8, 2020. The copyright holder for this preprint (which was not certified by peer review) is the author/funder, who has granted bioRxiv a license to display the preprint in perpetuity. It is made available under aCC-BY-ND 4.0 International license.

rank test). Punctate sensory mean +/- SEM control: 18.38 +/- 1.27 Hz, adapted: 6.59 +/- 0.65 Hz, 64.17% decrease, $p = 1.39 \times 10^{-12}$ N = 71 units, Wilcoxon signed-rank test. Punctate terminal mean +/- SEM control: 11.7 +/- 0.95 Hz, adapted: 11.38 +/- 0.99 Hz, 2.75% decrease, p = 0.19. D. Distributions of normalized adapted responses for all valid units (see Methods). Triangles at top denote population median values (***: $p < 0.001$, Wilcoxon signed-rank test). Population median normalized adapted response = -0.29 punctate terminal trials, 0.96 punctate sensory trials, $p = 3.12 \times 10^{-11}$, Wilcoxon signed-rank test. E. Left: experimental setup for in vivo S1 patch clamp recordings in lightly-anesthetized transgenic mice. Right: Across-trial median membrane potential responses to punctate sensory (black traces) and punctate terminal (blue traces) stimuli, for one example S1 neuron. F. Properties of subthreshold responses to punctate sensory (left) and punctate terminal (right) stimulation: subthreshold response amplitude (top), and time from stimulus onset to peak subthreshold response (T_{peak}, center) for each of the four recorded cells. Dark lines connecting pairs of data points indicate significant difference across stimulus conditions ($p < 0.05$, Wilcoxon signed-rank test), and light lines indicate non-significance.

Figure 8. A thalamocortical network model identifies synchronous VPm spikes and feedforward inhibition as key mechanisms underlying response adaptation. A. Model schematic (see Methods). B. Grand mean PSTHs for VPm spike times used to stimulate the network (top) and network excitatory and inhibitory neurons, for the control (empty PSTHs) and adapted (filled PSTHs) conditions. C. Population median normalized adapted responses for both simulated stimulus velocities (see Methods). Error bars indicate 95% confidence intervals from re-sampling with replacement. D. Grand exc-exc (left) and inh-inh (right) CCGs for 200 randomly-selected pairs of network neurons, for the control (dark line) and adapted (lighter line) conditions. CCGs normalized to max value in control condition for visualization purposes. E. Top: grand CCGs for VPm inputs to model in the control (dark line) and adapted (lighter line) conditions (corresponding to PSTHs in B, top). Bottom: grand CCGs for VPm inputs in the control (dark line) and "reduced synch" (lighter line) conditions, where the "reduced synch" condition results from

bioRxiv preprint doi: https://doi.org/10.1101/2020.10.08.331660; this version posted October 8, 2020. The copyright holder for this preprint (which was not certified by peer review) is the author/funder, who has granted bioRxiv a license to display the preprint in perpetuity. It is made available under aCC-BY-ND 4.0 International license.

manual changes to drawn VPm spike times (see Methods). F. Same as in B, but for control and “reduced synch“ simulations. G. Normalized “reduced synch“ response for simulations in (F). H. Same as in (D), but for simulations in (F). I. Model schematic for “identical TC connectivity” network (see Results and Methods). J. Grand excitatory (top) and inhibitory (bottom) PSTHs for “identical TC connectivity” network. K, L. Same as in (G, H), but for “identical TC connectivity” network.

Figure 1

bioRxiv preprint doi: https://doi.org/10.1101/2020.10.08.331660; this version posted October 8, 2020. The copyright holder for this preprint (which was not certified by peer review) is the author/funder, who has granted bioRxiv a license to display the preprint in perpetuity. It is made available under aCC-BY-ND 4.0 International license.

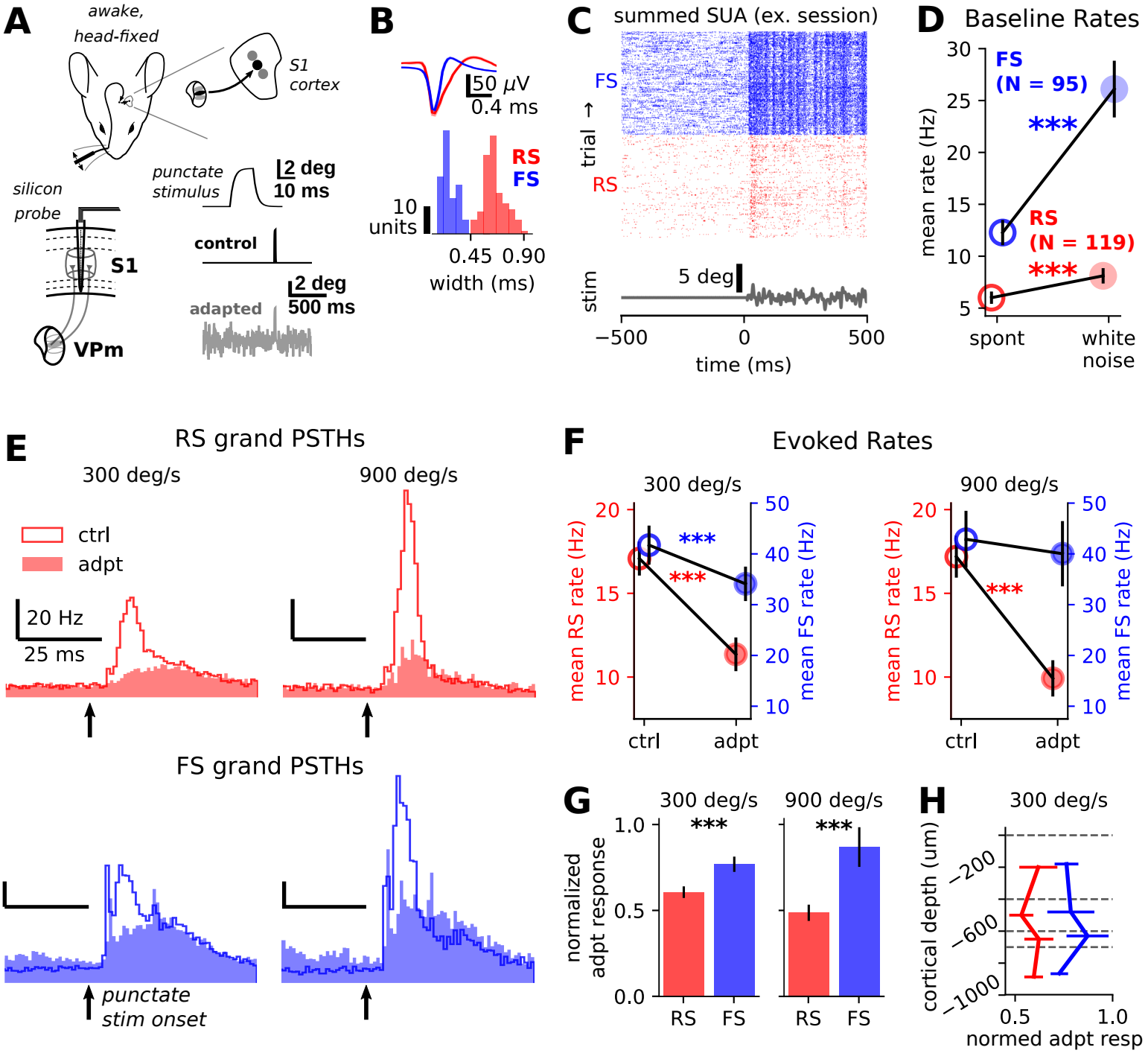

bioRxiv preprint doi: https://doi.org/10.1101/2020.10.08.331660; this version posted October 8, 2020. The copyright holder for this preprint (which was not certified by peer review) is the author/funder, who has granted bioRxiv a license to display the preprint in perpetuity. It is made available under aCC-BY-ND 4.0 International license.

Figure 2

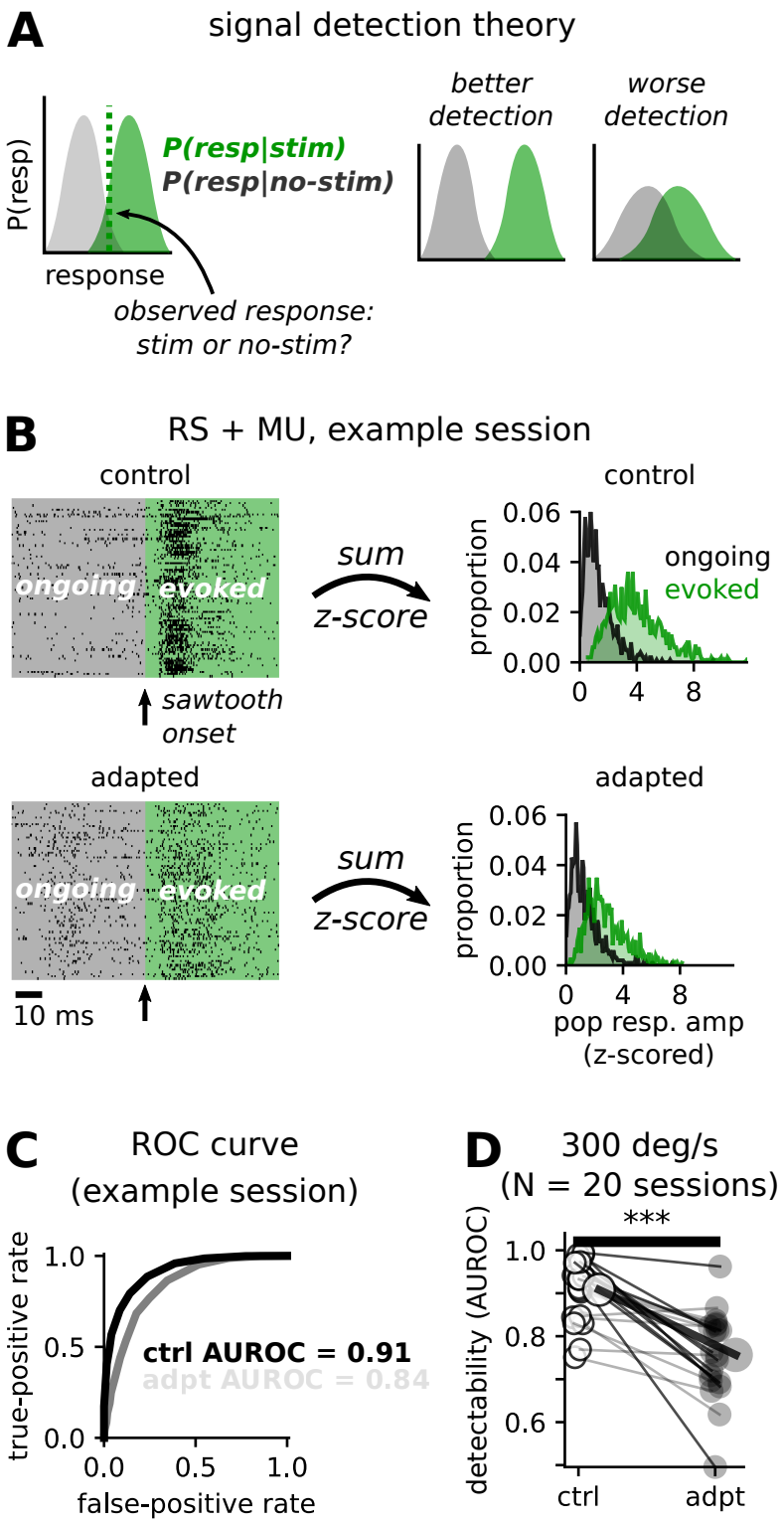

bioRxiv preprint doi: https://doi.org/10.1101/2020.10.08.331660; this version posted October 8, 2020. The copyright holder for this preprint (which was not certified by peer review) is the author/funder, who has granted bioRxiv a license to display the preprint in perpetuity. It is made available under aCC-BY-ND 4.0 International license.

Figure 3

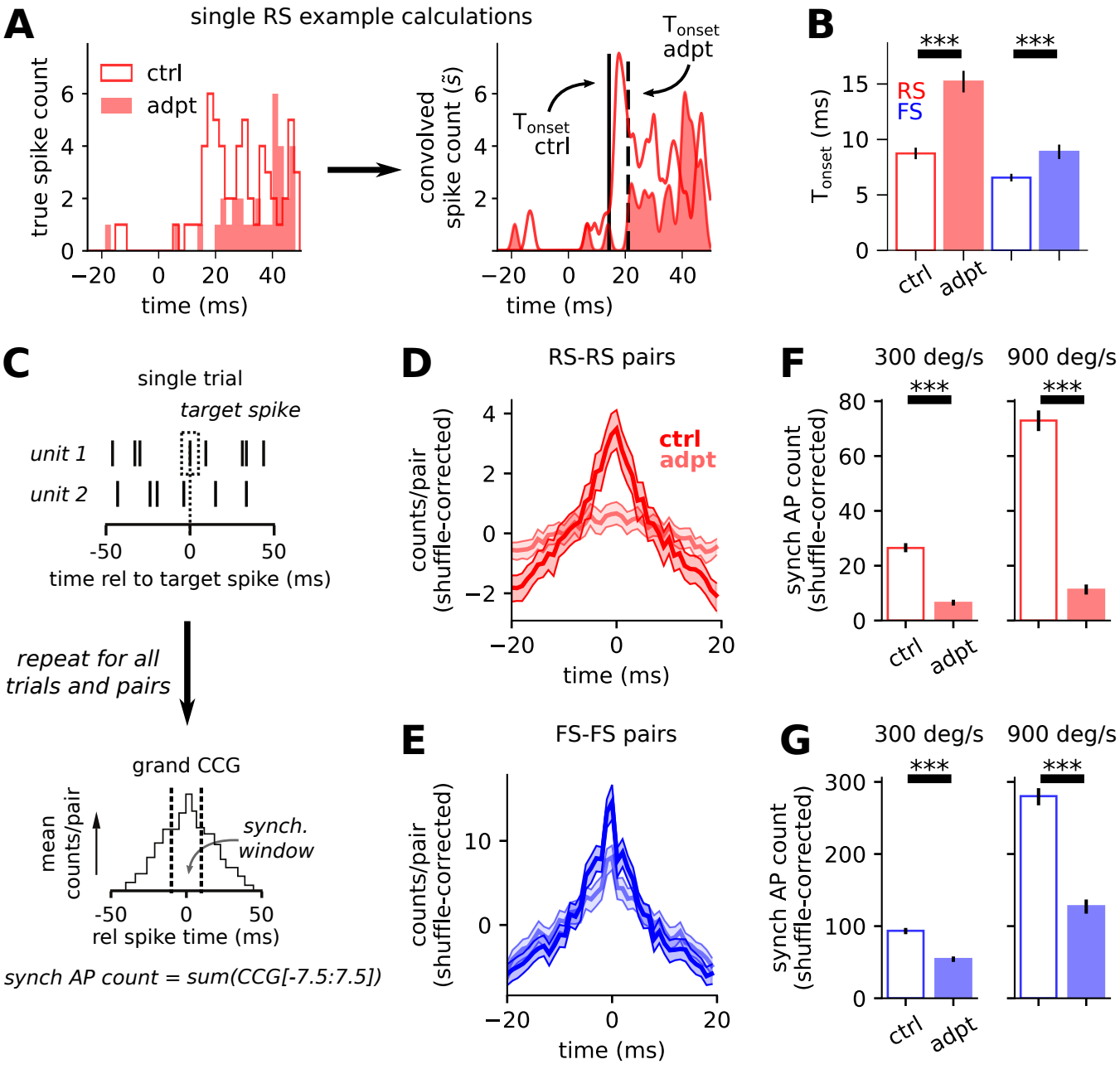

bioRxiv preprint doi: https://doi.org/10.1101/2020.10.08.331660; this version posted October 8, 2020. The copyright holder for this preprint (which was not certified by peer review) is the author/funder, who has granted bioRxiv a license to display the preprint in perpetuity. It is made available under aCC-BY-ND 4.0 International license.

Figure 4

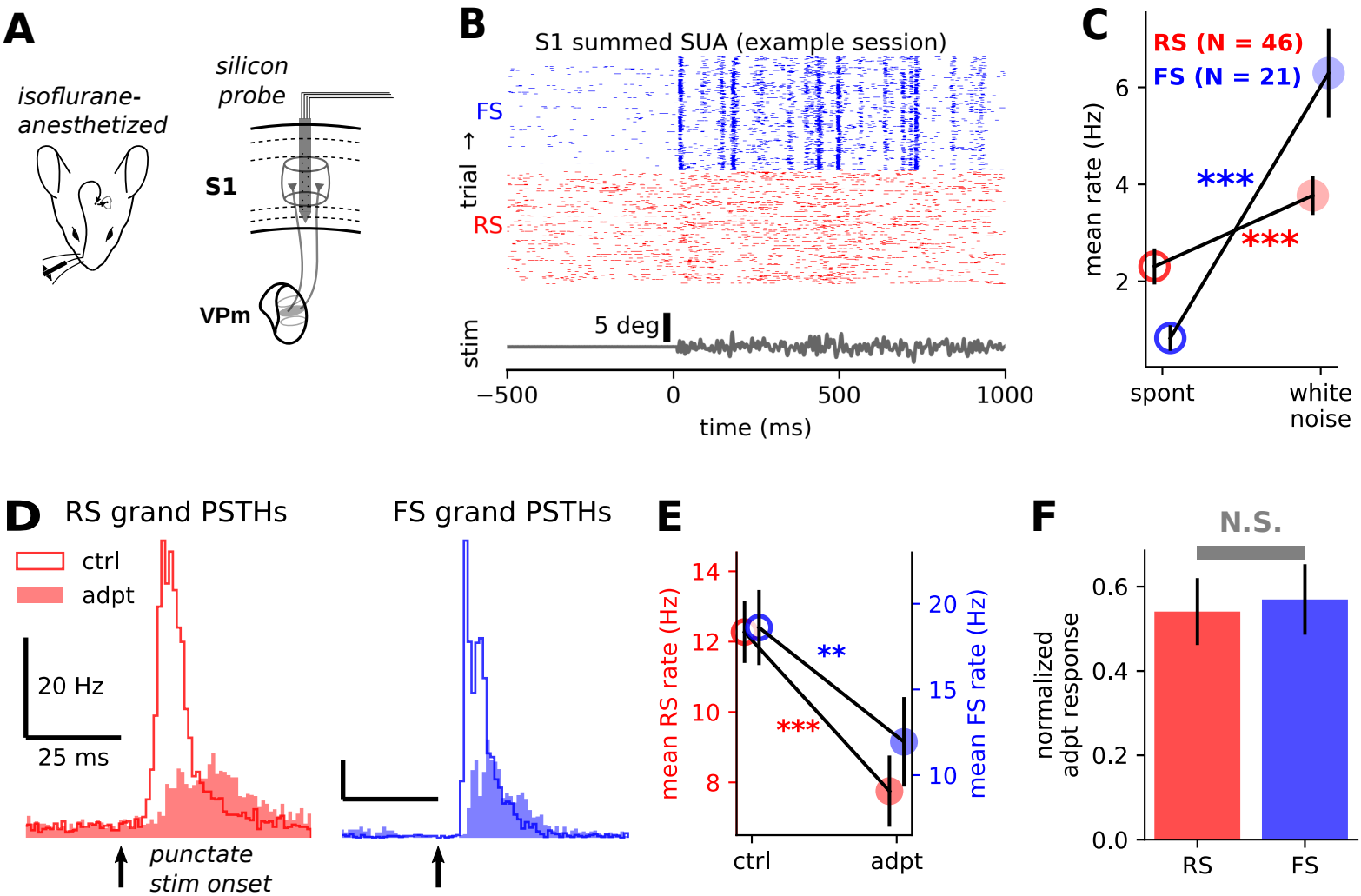

bioRxiv preprint doi: https://doi.org/10.1101/2020.10.08.331660; this version posted October 8, 2020. The copyright holder for this preprint (which was not certified by peer review) is the author/funder, who has granted bioRxiv a license to display the preprint in perpetuity. It is made available under aCC-BY-ND 4.0 International license.

Figure 5

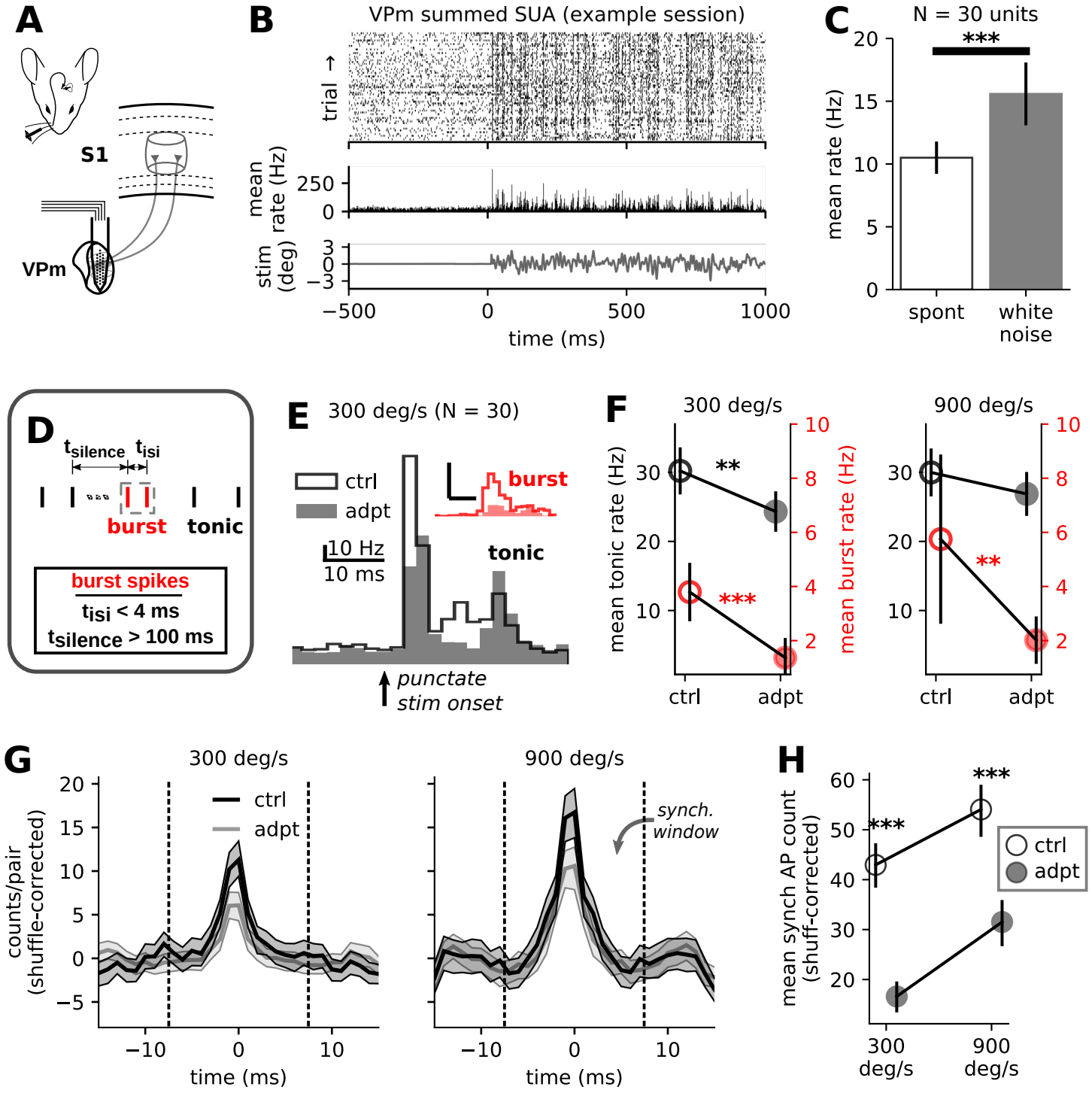

bioRxiv preprint doi: https://doi.org/10.1101/2020.10.08.331660; this version posted October 8, 2020. The copyright holder for this preprint (which was not certified by peer review) is the author/funder, who has granted bioRxiv a license to display the preprint in perpetuity. It is made available under aCC-BY-ND 4.0 International license.

Figure 6

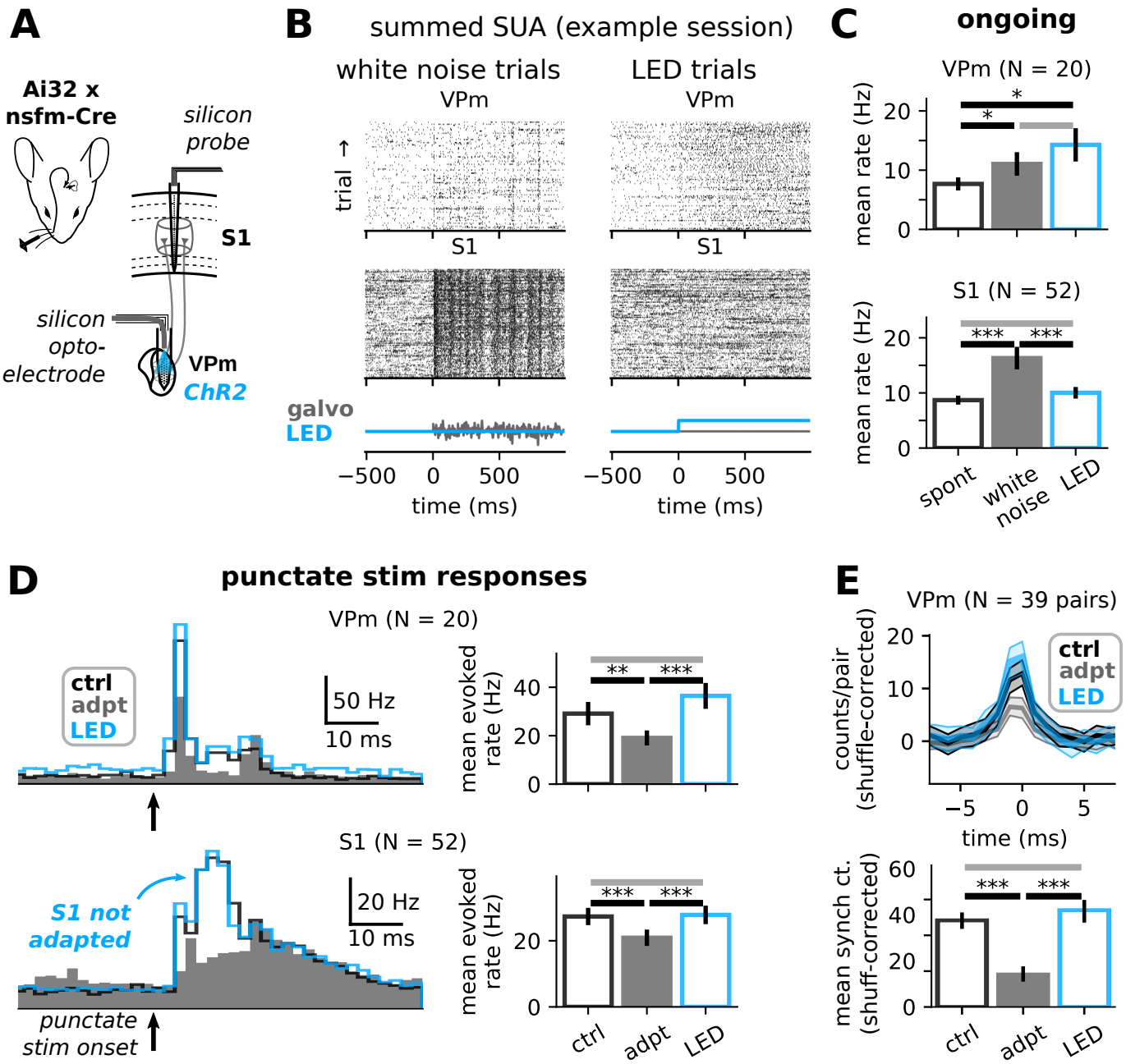

bioRxiv preprint doi: https://doi.org/10.1101/2020.10.08.331660; this version posted October 8, 2020. The copyright holder for this preprint (which was not certified by peer review) is the author/funder, who has granted bioRxiv a license to display the preprint in perpetuity. It is made available under aCC-BY-ND 4.0 International license.

Figure 7

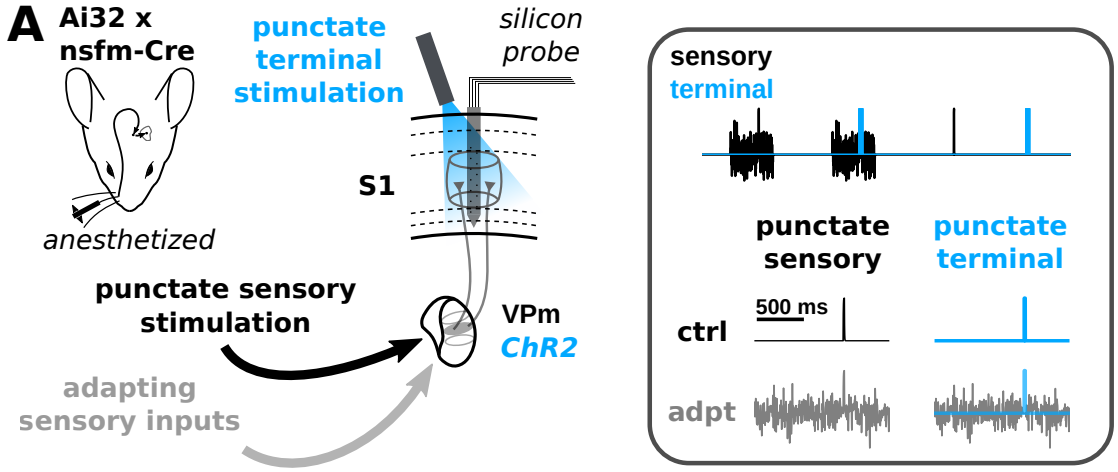

S1 grand PSTH (N = 71 SU + MU)

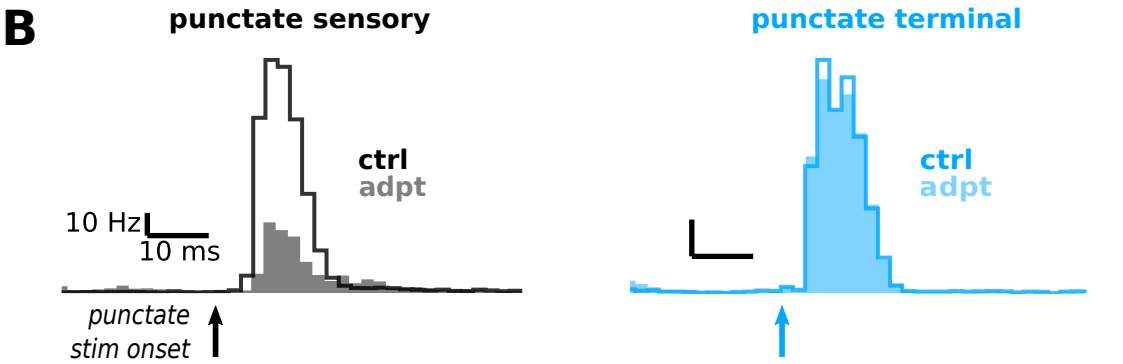

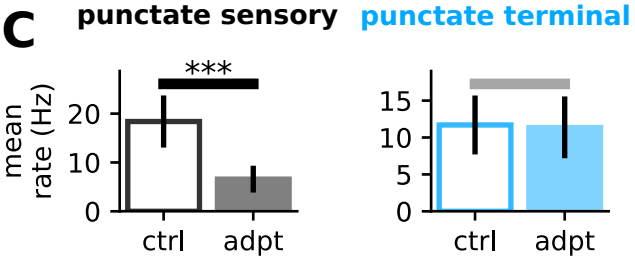

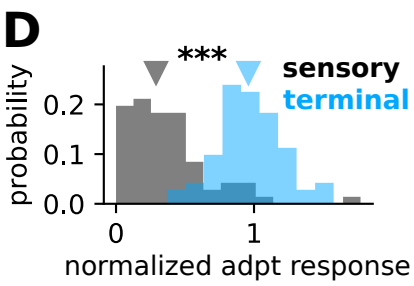

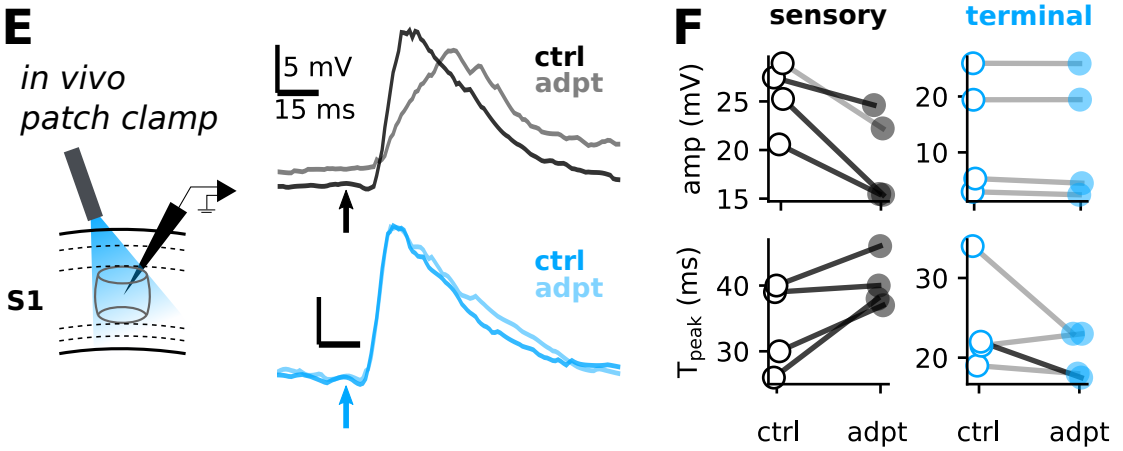

bioRxiv preprint doi: https://doi.org/10.1101/2020.10.08.331660; this version posted October 8, 2020. The copyright holder for this preprint (which was not certified by peer review) is the author/funder, who has granted bioRxiv a license to display the preprint in perpetuity. It is made available under aCC-BY-ND 4.0 International license.
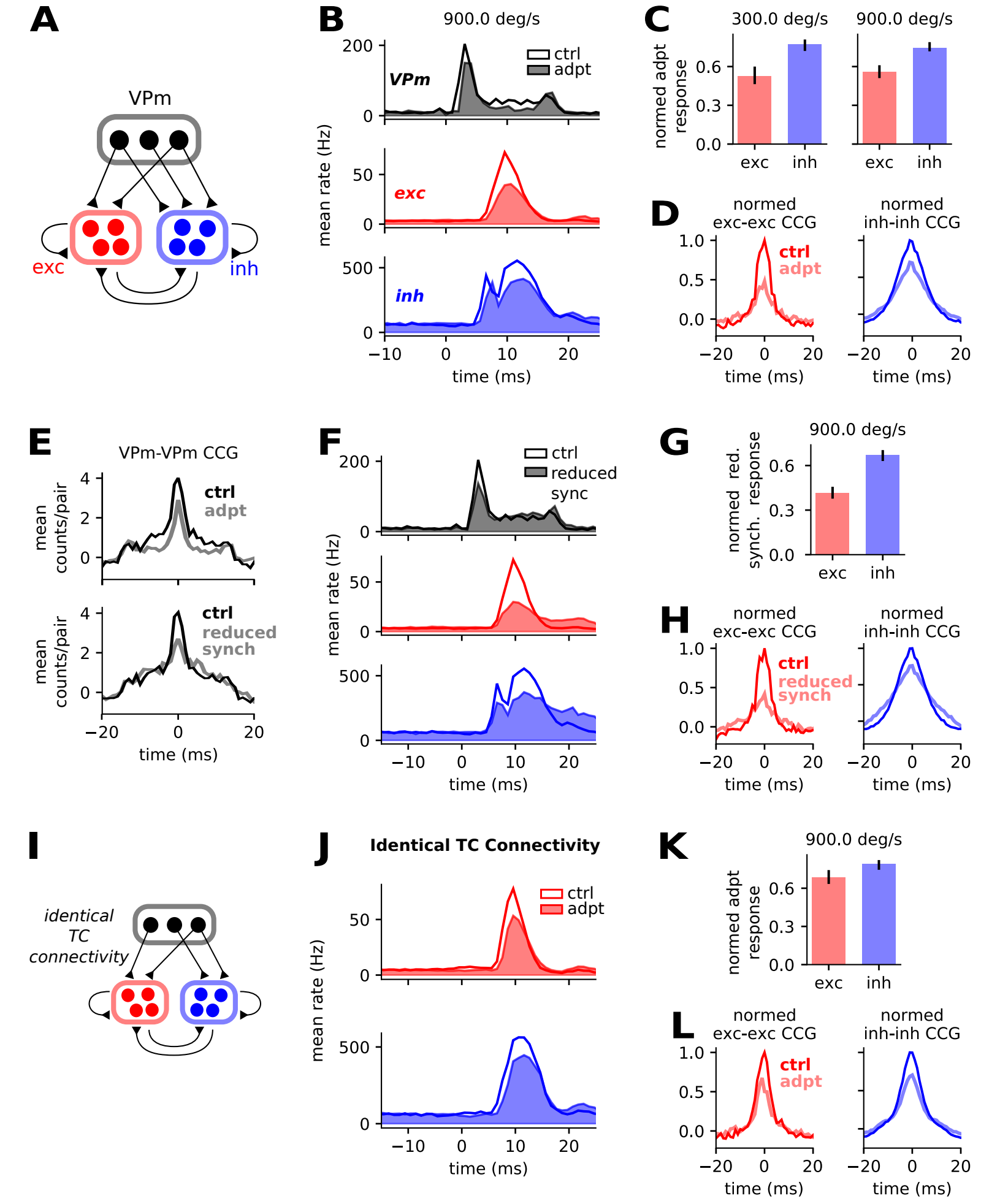
Figure 8